Available online at www.sciencedirect.com
SCIENCE DIRECT®
Geochimica et Cosmochimica Acta 70 (2006) 3905–3927
Geochimica
www.elsevier.com/locate/gca

Kinetics of organic matter degradation, microbial methane generation, and gas hydrate formation in anoxic marine sediments

K. Wallmann [a,*], G. Aloisi [b], M. Haeckel [a], A. Obzhirov [c], G. Pavlova [c], P. Tishchenko [c]

[a] *IFM-GEOMAR Research Center, Wischhofstrasse 1-3, 24148 Kiel, Germany*
[b] *Laboratoire de Paléoenvironnements et Paléobiosphère, Université Claude Bernard, Lyon I, 2, rue Dubois, F-69622 Villeurbanne cedex, France*
[c] *Pacific Oceanological Institute (POI), 43, Baltiyskaya Street, 690041 Vladivostok, Russia*

Received 28 February 2006; accepted in revised form 5 June 2006

Abstract

Seven sediment cores were taken in the Sea of Okhotsk in a south-north transect along the slope of Sakhalin Island. The retrieved anoxic sediments and pore fluids were analyzed for particulate organic carbon (POC), total nitrogen, total sulfur, dissolved sulfate, sulfide, methane, ammonium, iodide, bromide, calcium, and total alkalinity. A novel method was developed to derive sedimentation rates from a steady-state nitrogen mass balance. Rates of organic matter degradation, sulfate reduction, methane turnover, and carbonate precipitation were derived from the data applying a steady-state transport-reaction model. A good fit to the data set was obtained using the following new rate law for organic matter degradation in anoxic sediments:

$$R_{\mathrm{POC}} = \frac{K_{\mathrm{C}}}{C(\mathrm{DIC}) + C(\mathrm{CH_4}) + K_{\mathrm{C}}} \cdot k_x \cdot \mathrm{POC}$$

The rate of particulate organic carbon degradation (R_{POC}) was found to depend on the POC concentration, an age-dependent kinetic constant (k_x) and the concentration of dissolved metabolites. Rates are inhibited at high dissolved inorganic carbon (DIC) and dissolved methane (CH_4) concentrations. The best fit to the data was obtained applying an inhibition constant K_{C} of 35 ± 5 mM. The modeling further showed that bromide and iodide are preferentially released during organic matter degradation in anoxic sediments. Carbonate precipitation is driven by the anaerobic oxidation of methane (AOM) and removes one third of the carbonate alkalinity generated via AOM. The new model of organic matter degradation was further tested and extended to simulate the accumulation of gas hydrates at Blake Ridge. A good fit to the available POC, total nitrogen, dissolved ammonium, bromide, iodide and sulfate data was obtained confirming that the new model can be used to simulate organic matter degradation and methane production over the entire hydrate stability zone (HSZ). The modeling revealed that most of the gas hydrates accumulating in Blake Ridge sediments are neither formed by organic matter degradation within the HSZ nor by dissolved methane transported to the surface by upward fluid flow but rather through the ascent of gas bubbles from deeper sediment layers. The model was further applied to predict rates of hydrate accumulation in Sakhalin slope sediments. It showed that only up to 0.3% of the pore space is occupied by gas hydrates formed via organic matter degradation within the HSZ. Gas bubble ascent may, however, significantly increase the total amount of hydrate in these deposits.
© 2006 Elsevier Inc. All rights reserved.

1. Introduction

Degradation rates of particulate organic matter (POM) in marine surface sediments have been studied in detail over the past decades (Berner, 1980; Boudreau, 1997 and references therein). They decrease with age of the degrading POM and with sediment depth because labile fractions are preferentially consumed reducing the overall reactivity of the remaining POM fractions (Westrich and Berner, 1984). Various kinetic models have been introduced to consider the age effects on degradation rates. These include multi-G models where POM is divided into two or three

* Corresponding author.
E-mail address: kwallmann@ifm-geomar.de (K. Wallmann).

0016-7037/$ - see front matter © 2006 Elsevier Inc. All rights reserved.
doi:10.1016/j.gca.2006.06.003

fractions of different reactivity each being degraded with its own kinetic constant (Westrich and Berner, 1984; Boudreau, 1996b; Luff et al., 2000) and reactive continuum models, which consider sedimentary POM to be composed of an unlimited number of different fractions each having its own reactivity (Middelburg, 1989; Boudreau and Ruddick, 1991). The concentration of terminal electron acceptors used in microbial POM degradation (e.g., sulfate in anoxic marine sediments) are often considered in the kinetic equations applying Monod terms (Rabouille and Gaillard, 1991). It has also been shown that sedimentary organic matter degrades more efficiently under oxic than anoxic conditions (Hedges et al., 1999; Kristensen and Holmer, 2001). However, the concentrations of degradation products, such as methane or CO_2, accumulating in the pore waters of anoxic sediments were not taken into account even though simple thermodynamic reasoning (Le Chatelier's principle) would suggest that the gain in Gibb's free energy and, hence, the degradation rates should be diminished by the accumulation of metabolites.

The kinetics of POM degradation in anoxic sediments have recently gained renewed interest because methane gas hydrates are formed in these sedimentary environments often by microbial rather than thermogenic degradation processes (Kvenvolden and Lorenson, 2001). Gas hydrates might have had a significant effect on the global carbon cycle and climate of the geological past if they are indeed as abundant as commonly assumed (Dickens et al., 1995). However, an updated estimate of global hydrate abundance gave very low numbers suggesting that the effects of hydrates on climate might have been grossly over-stated (Milkov, 2004). State-of-the-art models of biogenic methane and hydrate formation use rather simple kinetic formulations (Rempel and Buffett, 1998; Davie and Buffett, 2001, 2003a). They have been applied to estimate the global abundance of biogenic gas hydrates in marine sediments (Buffett and Archer, 2004; Archer and Buffett, 2005). The outcome of these models may, however, be significantly enhanced applying improved rate laws for POM degradation.

Anoxic marine sediments occur along productive continental margins. Methane formation rates are especially high where sedimentation rates are enhanced by the delivery of fine-grained riverine particles. The north-eastern slopes of Sakhalin Island are an important example for this kind of setting. The productivity of the area located in the northern Sea of Okhotsk is very high and the adjacent Amur River delivers abundant clay minerals so that slope sediments composed of fine-grained terrigenous matter, biogenic opal and POM accumulate at high rates. Sedimentation rates are as high as 1 m kyr^{-1} and seismic data indicate the occurrence of gas hydrates (Lüdmann and Wong, 2003).

In this paper, we present and evaluate sediment and pore water data from the slope of Sakhalin Island. We demonstrate that rates of sulfate reduction and methane generation depend not only on the reactivity of buried POM but also on the concentrations of methane and dissolved inorganic carbon prevailing in the pore waters of these organic matter-rich deposits. Based on these observations, we develop a new kinetic rate law for the degradation of organic matter in anoxic sediments. Subsequently, this rate law is further tested and applied to simulate gas hydrate formation in Blake Ridge and Sakhalin slope sediments.

2. Study area

Sedimentary processes in the Sea of Okhotsk were intensively studied within the joint Russian-German project KOMEX (Kurile-Okhotsk Sea Marine Experiment). Sakhalin Island is situated at the north-western boundary of the Sea of Okhotsk, a large marginal sea located in the north-western Pacific (Fig. 1). During the cold season, the Sea of Okhotsk is largely covered with sea-ice. Primary production is low during winter and summer but very intense during spring and autumn (Broerse et al., 2000). The spring bloom is dominated by diatoms whereas the autumn peak is mainly caused by calcareous plankton. During spring and early autumn, primary production calculated from remote sensing data is high with an average of 120–160 g C m^{-2} y^{-1} (Antoine et al., 1996). The annual export production derived by inverse modeling of nutrient and oxygen profiles in the water column amounts to more than 72 g C m^{-2} y^{-1} (Schlitzer, 2000). The East Sakhalin Current flows southwards along the Sakhalin coast transporting cold surface waters and Amur River water from north to south. The northern slope and shelf of Sakhalin Island are strongly influenced by fresh water and sediment input from the adjacent Amur. Here, primary production is at its maximum and may reach values of up to 250 g C m^{-2} y^{-1} during the warm season (Antoine et al.,

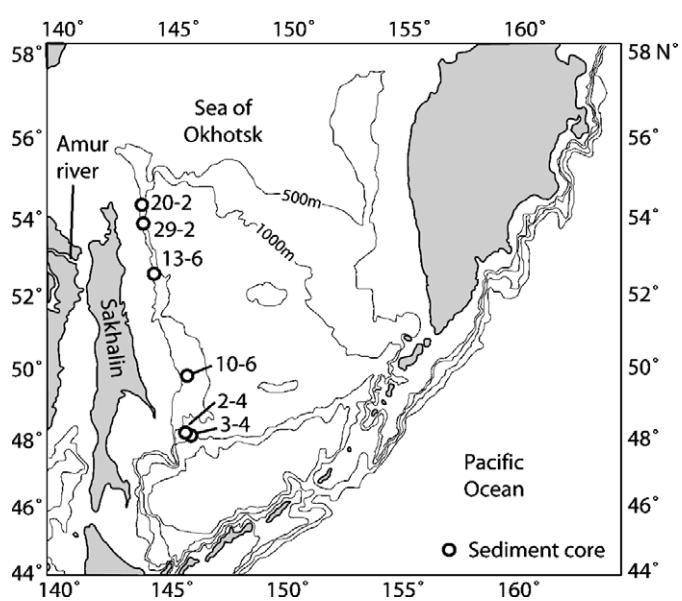

Fig. 1. Map of the study area and sampling sites (3-4, SO178 3-4 KAL; 2-4, LV28 2-4 SL; 10-6, SO178 10-6 SL; 13-6, SO178 13-6 KL; 29-2, SO178 29-2 KL; 20-2, LV28 20-2 KL).

1996). Sedimentation is dominated by biogenic opal and terrigenous inputs from the Amur River. The Holocene sedimentation rates are as high as 100 cm ky^{-1} in the northern slope area and decrease towards the south by one order of magnitude (Wong et al., 2003).

Gas hydrates, free gas and mud diapirism have been imaged by seismic reflection data (Lüdmann and Wong, 2003). The total amount of methane preserved in the hydrate stability zone and trapped as free gas beneath the bottom simulating reflector (BSR) was estimated to $17 \pm 14 \times 10^{12}$ m^3 for the north-western Sea of Okhotsk (Lüdmann and Wong, 2003). A BSR—marking the boundary between the hydrate stability zone and underlying gas-bearing sediments—was found throughout the entire northern slope area off Sakhalin Island (Lüdmann and Wong, 2003). Hydro-acoustic anomalies ("flares") caused by rising methane gas bubbles and enhanced methane concentrations in bottom waters demonstrate active gas venting processes at numerous sites along the northern slope (Obzhirov et al., 2004). Methane gas hydrates were sampled repeatedly in surface sediments of active vent sites at the northern slope area and stable isotopic data indicate their dominantly biogenic origin (Ginsburg et al., 1993; Matveeva et al., 2003).

3. Sampling and analytical techniques

Samples were taken during joint Russian-German expeditions with *RV Akademik M. A. Lavrentyev* in August–September 1998 (LV28) and *RV SONNE* in July–September 2004 (SO178). Sediments were taken using different coring techniques and instruments including a gravity corer (SL), a piston corer (KL), and a Kasten corer (KAL). Core recovery was 5–24 m, depending on location and coring gear (see Table 1 and Fig. 1).

Sediment cores were cut into meter pieces and stored in the cold room at 4 °C. Subsequently, they were opened with a saw and immediately sub-sampled every 0.1–1 m. At each depth position, 50 cm^3 of wet sediment were taken for pore water sampling, and 5 cm^3 for the determination of physical properties (water content, porosity). Wet sediments were also transferred to gas-tight vials to determine the methane concentration using the head-space technique (Niewöhner et al., 1998). Pore waters were separated from the sediment matrix via squeezing in a cold room at 4 °C temperature and 2–4 bar using a polypropylene apparatus pressurized by argon and equipped with 0.45 μm cellulose acetate membrane filters. All vials used for pore water storage were previously washed with acid and Milli-Q water to prevent sample contamination. As pore water samples rapidly lose alkalinity and Ca during storage, these parameters were determined within a few hours after sampling while sub-samples for sulfide determination were taken within two hours after squeezing and conserved with zinc-acetate solution.

Table 1
List of coring stations in geographic order going from south to north along the Sakhalin slope

Station	Location	Water depth (m)	Recovery (m)
SO178 3-4 KAL	48°11.83′N 146°08.74′E	1602	10.0
LV28 2-4 SL	48°22.73′N 146°02.22′E	1265	6.0
SO178 10-6 SL	49°44.88′N 146°00.48′E	613	11.5
SO178 13-6 KL	52°43.88′N 144°42.65′E	713	23.7
SO178 29-2 KL	53°50.00′N 144°14.23′E	771	24.3
LV28 20-2 SL	54°26.52′N 144°04.09′E	685	5.9

Samples for dissolved calcium (Ca) in pore water were analyzed by complexometric titration of 1 ml of pore water dispensed in 10 ml de-ionized water (Grasshoff et al., 1983). The Brinkman/Dosimat 665 motor-driven piston burette reproducible to ±0.001 ml in the delivered volume was applied for analysis. Based on analysis in pore water replicates analytical precision of ±7 μmol/kg ($n = 8$) for calcium in pore water was achieved in this study. Ca was also measured using ICP-AES. The results of the two-independent methods usually agreed within 1% when the titration was performed within a few hours after sampling and when sub-samples for on-shore ICP-AES analysis were taken and acidified within the same short period of time. Prolonged storage without acid addition reduced the dissolved Ca concentrations significantly due to $CaCO_3$ precipitation.

Samples for total alkalinity (TA) in pore water were analyzed by direct titration in an open cell of 1 ml of pore water dispensed in 10 ml deionized water with 0.02 N HCl using Bruevich's method (Ivanenkov and Lyakhin, 1978). The acid was standardized daily with Na_2CO_3 solution prepared from crystals dried at 280 °C and dissolved in CO_2-free deionized water. To remove CO_2 and H_2S during titration, the samples and standards were flushed with a continuous stream of pure nitrogen. A mixture of methylene blue and methyl red was used as indicator and titration was completed when the green color of the solution turned to light-pink (pH of the end point is equal to 5.4–5.5). The method is convenient to work with small sample volumes and avoids the errors caused by H_2S oxidation during titration. Replicate measurements ($n = 8$) indicated an analytical precision of ±10 μmol/kg for total alkalinity in pore waters. Replicate measurements of pore water samples over a time span of several hours revealed that the total alkalinity of anoxic pore water samples is not stable but decreases with time. The two most important reactions that cause alkalinity reduction are carbonate precipitation and sulfide oxidation. Carbonate precipitation is induced by the loss of CO_2 and H_2S from the pore waters to the atmosphere and the resulting shift in the dissolution/precipitation equilibrium. Sulfide oxidation consumes alkalinity via acid production. The sulfide oxidation rate and its impact on total alkalinity were tested under shipboard conditions using a 30 mM solution of Na_2S in 0.5 M NaCl. The initial pH was adjusted to 7.1 with concentrated HCl and the solution was titrated repeatedly at room temperature (24–25 °C). The data showed that total alkalinity is reduced by about

5% within a few hours. Thus, total alkalinity of anoxic samples was determined as fast as possible (within 2 h) after pore water retrieval.

Sulfide samples were conserved with zinc acetate gelatin solution (23.8 mM in Zn acetate) adding 4 ml solution to 1 ml pore water. The gelatin inhibits the precipitation of sulfide by fixing sulfide in a colloidal ZnS solution. The resulting colloidal solution was mixed with 40 μl phenylene-diamine and 40 μl $FeCl_3*6H_2O$ and the absorbance was measured after 10 min to 1 h at 670 nm using a Hitachi UV/VIS Spectrometer. A linear calibration curve was obtained in the concentration range of 0–57 μM ΣH_2S. The sulfide standard solution was titrated with sodium thiosulfate to determine the true concentration of the standard. Samples were diluted into the calibration range before reagent addition.

Dissolved ammonium was measured applying a standard photometric procedure on a Hitachi UV/VIS Spectrometer. The analysis of nutrient concentrations was disturbed in anoxic samples with high ΣH_2S concentrations. Thus, sulfide-bearing samples were acidified with HCl (20 μl conc. HCl per 3 ml sample) and bubbled with nitrogen gas prior to analysis. By this procedure sulfide was converted into hydrogen sulfide and stripped from the solution. For the ammonium determination, 1 ml water sample or standard were diluted with 4 ml Milli-Q water and 0.2 ml phenol solution were added. After 2 min 0.1 ml citrate buffer and 0.2 ml DTT reagent were added and the samples were kept at room temperature protected from sunlight for about 24 h before the absorbance was measured at 630 nm.

Dissolved chloride, bromide, iodide, and sulfate were determined using ion-chromatography. We used a Methrom ion-chromatograph equipped with a conventional anion-exchange column and carbonate-bicarbonate solution as solvent. UV-detection was used for the determination of iodide while a conductivity sensor was applied for the measurement of the other anions. Standard deviations were found to be 1% for chloride, 2% for sulfate, and 5% for bromide and iodide.

Squeezed sediment samples were freeze-dried and ground in an agate mortar for further analysis. Desalting with distilled water was avoided because this procedure reduces the C and S contents of the solids due to the leaching of dissolved organic carbon and oxidized sulfur compounds. The chloride contents in dried and ground aliquots were determined by extraction with distilled water and titration with $AgNO_3$ solution to calculate the contribution of dissolved and exchangeable salts to the total mass and to the total sulfur content. The fine-grained sediments contained 2–3 wt% Cl mainly as exchangeable ion (Sayles and Mangelsdorf, 1977) whereas the sand sediments usually contained less than 0.5 wt% Cl from desiccated pore water. In this paper, the exchangeable salts are regarded as integral part of the solid sediment and the small salt contribution from pore water preserved after squeezing was ignored in the calculation of dry weights and solid phase concentrations. Only the sulfur data were corrected because pore water and exchangeable sulfate contributed significantly to the total sulfur in dried samples. The sulfate content was calculated using the sulfur/chlorine ratio previously determined in the corresponding pore water sample and the chloride concentration in the dried sample. It was subtracted from the sulfur concentration in dried sediments to calculate the sulfur concentrations in the solid phase.

Total C, N, and S were determined by combustion of squeezed sediment samples and gas-chromatographic detection of CO_2, N_2, and SO_2 produced in the combustion process using a Carlo-Erba element analyzer (NA 1500). Additional samples were repeatedly acidified with HCl and desiccated till complete dryness to release CO_2 from carbonate minerals. The residues were analyzed for C to determine the contents of particulate organic carbon. The carbonate content was determined from the difference between total and organic carbon. Sediment and soil standards with certified concentrations of C, N, and S were analyzed during each run (marine sediment MAG-1, United States geological Survey; soil standard 1, HEKAtech GmbH). The recovered values were always within the certified range. Replicate measurements of sediment samples ($n = 5$) revealed the following relative standard deviations: POC: 1%; $CaCO_3$: 2%; N: 3%; and S: 5%.

4. Numerical modeling procedure

A numerical transport-reaction model was developed and applied to simulate the degradation of particulate organic matter (POM) in anoxic marine sediments. The model calculates the concentration–depth profiles of 3 solid species (particulate organic carbon, particulate organic nitrogen, and adsorbed ammonium) and 7 dissolved species (sulfate, methane, ammonium, bromide, iodide, dissolved inorganic carbon, and calcium). Major processes considered in the model are POM degradation via sulfate reduction, methanogenesis, anaerobic oxidation of methane (AOM), carbonate precipitation, and ammonium adsorption. A detailed description of the model is given in Appendix A.

Partial differential equations for solids and solutes were set-up following the classical approach used in early diagenesis modeling:

Solutes:

$$\Phi \cdot \frac{\partial C}{\partial t} = \frac{\partial\left(\Phi \cdot D_S \cdot \frac{\partial C}{\partial x}\right)}{\partial x} - \frac{\partial(\Phi \cdot v \cdot C)}{\partial x} + \Phi \cdot R, \quad (1)$$

Solids:

$$(1-\Phi) \cdot \frac{\partial G}{\partial t} = -\frac{\partial((1-\Phi) \cdot w \cdot G)}{\partial x} + (1-\Phi) \cdot R, \quad (2)$$

where x is depth, t is time, Φ is porosity, C is the concentration of dissolved species in pore water, v is the burial velocity of solutes, G is the concentration of solids in dry

sediments, w gives the burial velocity of solids, and R defines the reactions occurring in the simulated sediment column. The model considers the decrease in porosity with sediment depth, advective transport of solutes and solids via burial and steady-state compaction, molecular diffusion of dissolved species and various microbial and chemical reactions.

The sampling gear and the sub-sampling procedure adopted in our study are not well suited to resolve concentration gradients within the top few decimeters of the sediment column where the transport of solids and solutes is accelerated by bioturbation and bioirrigation. Hence, these biogenic transport processes were neglected in the modeling. Our data showed steep concentration gradients between the uppermost sampling points and no indication of deep reaching mixing thus confirming our modeling approach (Figs. 2–7).

A novel rate law was introduced to describe the effect of metabolite concentrations on the anaerobic degradation of particulate organic carbon (POC) in anoxic marine sediments:

$$R_{\mathrm{POC}} = \frac{K_{\mathrm{C}}}{C(\mathrm{DIC}) + C(\mathrm{CH_4}) + K_C} \cdot k_x \cdot \mathrm{POC}, \tag{3}$$

where R_{POC} is the POC degradation rate, $C(\mathrm{DIC})$ is the concentration of dissolved inorganic carbon ($CO_3 + HCO_3 + CO_2$) in the considered depth interval, $C(CH_4)$ is the ambient methane concentration in pore waters, k_x is an age-dependent kinetic constant, POC is the POC concentration and K_{C} is a Monod constant describing the inhibition of POC degradation by DIC and CH_4. The age effects on POC degradation are considered using the approach introduced by Middelburg (1989). Ages were calculated from sediment depth and burial rate. The rate law predicts that the microbial degradation of organic matter is inhibited by metabolites accumulating in adjacent pore fluids since the Gibb's free energy available for the microbial metabolism is reduced in the presence of high concentrations of reaction products.

A new approach was developed to derive sedimentation rates from a nitrogen mass balance at steady-state. The fluxes of total particulate nitrogen and dissolved ammonium at sediment depths below the bioturbated and bio-irrigated zones are given by:

Flux of N:

$$J_{\mathrm{PN}} = \Phi \cdot w \cdot r(\mathrm{N}) \cdot N, \tag{4}$$

Flux of NH_4:

$$J_{\mathrm{NH_4}} = \Phi \cdot \left(v \cdot C(\mathrm{NH_4}) - D_{\mathrm{S}} \cdot \frac{\mathrm{d}C(\mathrm{NH_4})}{\mathrm{d}x} \right), \tag{5}$$

where J is the flux (in mmol N $\mathrm{cm^{-2}\,yr^{-1}}$), N is the concentration of total particulate nitrogen including both adsorbed ammonium and organic nitrogen in wt%, r (N) is a unit conversion factor for solids defined in the appendix (see Table A1), and $C(NH_4)$ is the ammonium concentration in pore waters (in mmol $\mathrm{cm^{-3}}$). Considering two different sediment layers situated at shallow depth ($x = S$) and close to the base of the core ($x = L$), the mass balance for nitrogen at steady-state reads as:

$$J_N(S) - J_N(L) + J_{\mathrm{NH_4}}(S) - J_{\mathrm{NH_4}}(L) = 0. \tag{6}$$

Inserting the flux definition into the mass balance and considering also the definitions given in Table A1, an equation for the sedimentation rate w_f can be derived as:

$$w_f = \frac{D_{\mathrm{M}} \cdot \left(\frac{\mathrm{d}C(\mathrm{NH_4})}{\mathrm{d}x}(L) \cdot \Phi(L)^3 - \frac{\mathrm{d}C(\mathrm{NH_4})}{\mathrm{d}x}(S) \cdot \Phi(S)^3 \right)}{\frac{d_{\mathrm{S}} \cdot (1-\Phi_f) \cdot (N(L) - N(S))}{1.4} + \Phi_f \cdot (C(\mathrm{NH_4})(L) - C(\mathrm{NH_4})(S))}, \tag{7}$$

where D_{M} is the coefficient for molecular diffusion of ammonium ($\mathrm{cm^2\,yr^{-1}}$), d_{s} is the density of dry solids (2.5 g $\mathrm{cm^{-3}}$) and Φ_{f} is porosity at large depth (see Appendix A for further definitions). Appropriate functions are fitted through the data so that porosity, N and ammonium concentrations and the first derivative of $C(NH_4)$ with respect to depth can be derived from the data at two different depth positions (S an L) and inserted into the equation to yield sedimentation rates for each of the investigated cores (in cm $\mathrm{yr^{-1}}$).

A simple exponential function was used for data fitting:

$$y = y_f + (y_0 - y_f) \cdot \mathrm{e}^{-a \cdot x}, \tag{8}$$

where y is the depth-dependent variable (porosity, ammonium, N), y_f and y_0 are the values of the variables at large depth and at the surface, respectively, and a is an attenuation coefficient. Sedimentation rates derived by this novel approach are very suitable for steady-state modeling because they are internally consistent with the model assumptions.

Constant concentrations of dissolved species were prescribed at the upper and lower boundary of the model column (Dirichlet boundary conditions) while the vertical distribution of solids was simulated applying Dirichlet conditions at the upper boundary. The upper boundary of the model domain is situated not directly at the sediment/water interface but at the transition between oxic and suboxic surface layers affected by bioturbation and bioirrigation and the underlying anoxic sediment column. Undisturbed surface sediments were collected with a multi-corer along the Sakhalin slope and pore water analysis revealed nitrate penetration depths of only 2–8 cm (Biebow and Hütten, 2000). Hence, anoxic conditions prevailed already at shallow sediment depths. In most sediment cores we found significant gradients of dissolved species at the lower boundary indicating that dissolved species released in deeper sediment horizons were transport to the surface via diffusion. We applied Dirichlet rather than imposed flux (Neumann) conditions at the lower boundary to consider the effect of these solutes on the simulated pore water profiles. Concentrations of dissolved species used as boundary values were taken from our data set using samples taken at the uppermost and deepest points of the studied sediment

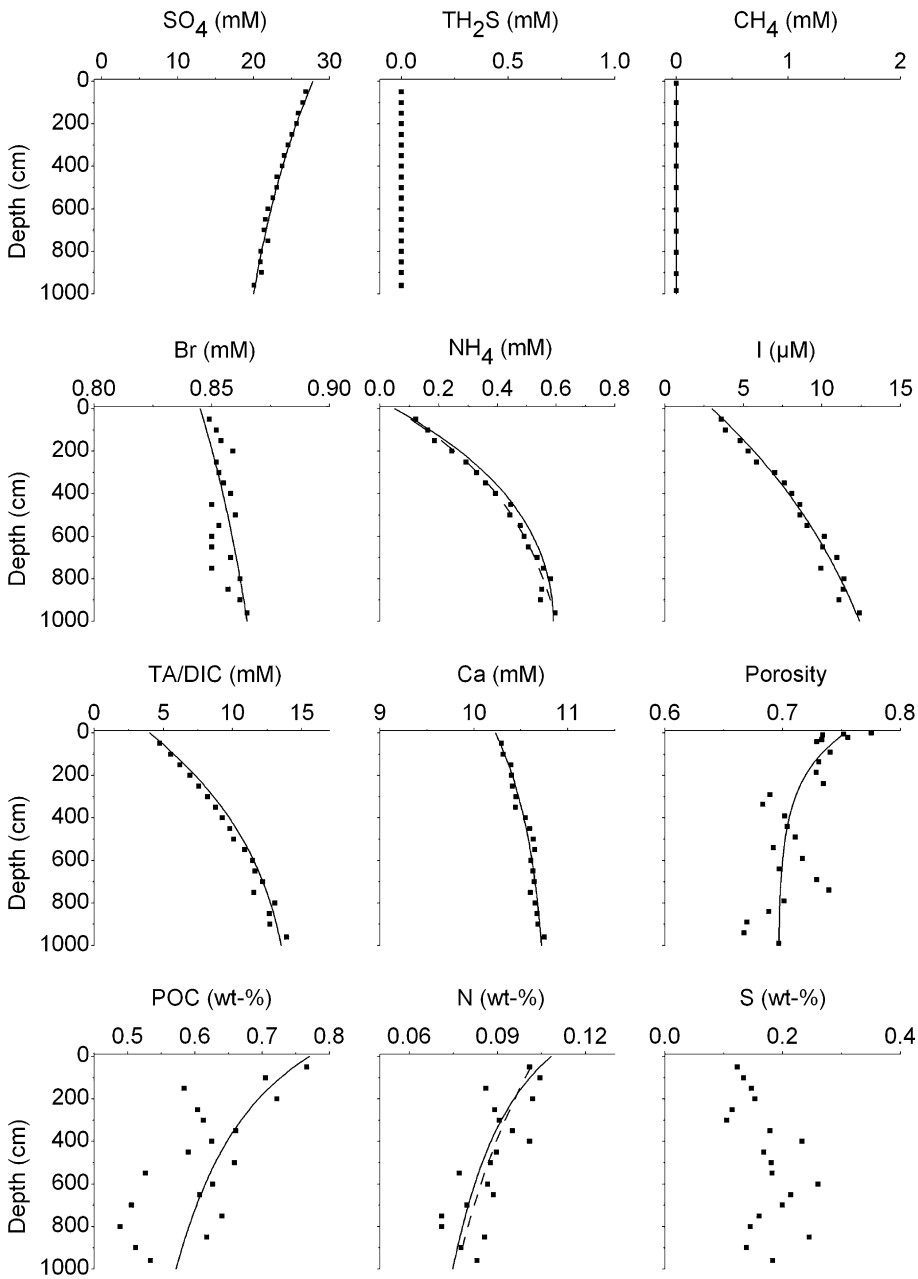

Fig. 2. Data (solid squares) and model results (solid lines) for core SO178 3-4 KL. Top row: Concentrations of sulfate (SO_4), total dissolved sulfide ($TH_2S = H_2S + HS^-$) and methane (CH_4) in pore water. Second row: Concentrations of bromide (Br), ammonium (NH_4) and iodide (I) in pore water. Third row: Concentrations of dissolved inorganic carbon ($DIC = CO_3^{2-} + HCO_3^- + CO_2$) calculated in the model, total alkalinity ($TA \approx HCO_3^- + 2CO_3^{2-} + HS^-$) measured in pore fluids, dissolved calcium (Ca) in pore water, and porosity of bulk sediments. Bottom row: Concentrations of particulate organic carbon (POC), total nitrogen (N = organic N + adsorbed NH_4) and total sulfur (S) in sediments. Pore water concentrations are given in mmol dm^{-3} (mM) or μmol dm^{-3} (μM) and are related to the pore water volume while solid phase concentrations are given in weight-percent (wt%) with respect to the weight of dry solids. The broken lines represent functions fitted through the ammonium and total nitrogen data to derive sedimentation rates.

cores. Upper boundary values for solids were also taken from the data.

Finite difference techniques (the method-of-lines code) which have been successfully applied in previous models of early diagenesis (Boudreau, 1996b; Luff et al., 2000; Luff and Wallmann, 2003) were used to solve the model. The set of 10 partial differential equations defining the model (one for each species) is converted into a large number of ordinary differential equations (ODE) giving the temporal change of species concentrations at each depth interval. A centered finite difference scheme was used for dissolved species while an upward scheme was applied for the transport of solids. The ODE system was set-up on an uneven grid with high resolution at the surface. It was solved and run into steady-state using the NDSolve object of MATHEMATICA Version 5. A

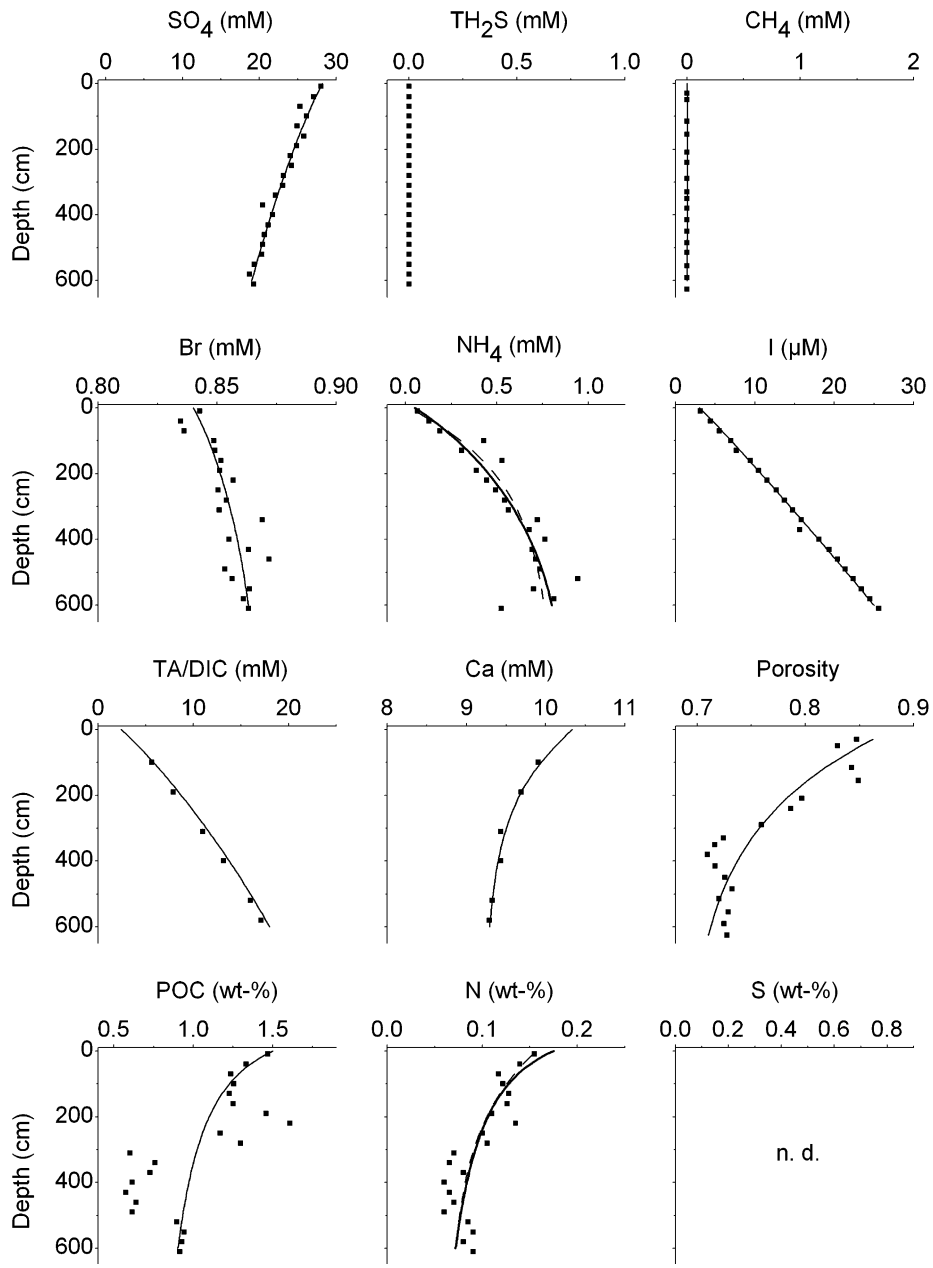

Fig. 3. Data (solid squares) and model results (solid lines) for core LV28 2-4 SL. For further information see legend of Fig. 2.

typical model run took about one minute on a Pentium 4 PC. MATHEMATICA notebooks containing the complete model code can be obtained from the first author upon request.

5. Results and discussion

5.1. Sedimentation rates

Patterns and rates of sedimentation in the Sea of Okhotsk rates have been studied by sediment coring (Gorbarenko et al., 2002) and seismic stratigraphy (Lüdmann and Wong, 2003; Wong et al., 2003). These studies show that Holocene sedimentation rates are as high as 50–140 cm kyr^{-1} at the northern Sakhalin slope and decrease by about one order of magnitude towards the southern slope area. On-board observations during cruise SO178 confirmed these general trends (Dullo et al., 2004). In the southernmost core SO178 3-4 KL, a tephra layer (K2, age 26 kyr) was found at a sediment depth of 153 cm indicating a sedimentation rate of about 6 cm kyr^{-1}. Considering, however, that the upper decimeters of this particular core were lost during coring, the sedimentation rate is probably higher than indicated by the uncorrected depth of the tephra layer. In core SO178 10-6 SL located further to the northern, the upper 200–220 cm of the sediment column were probably deposited during the Holocene indicating a sedimentation rate of

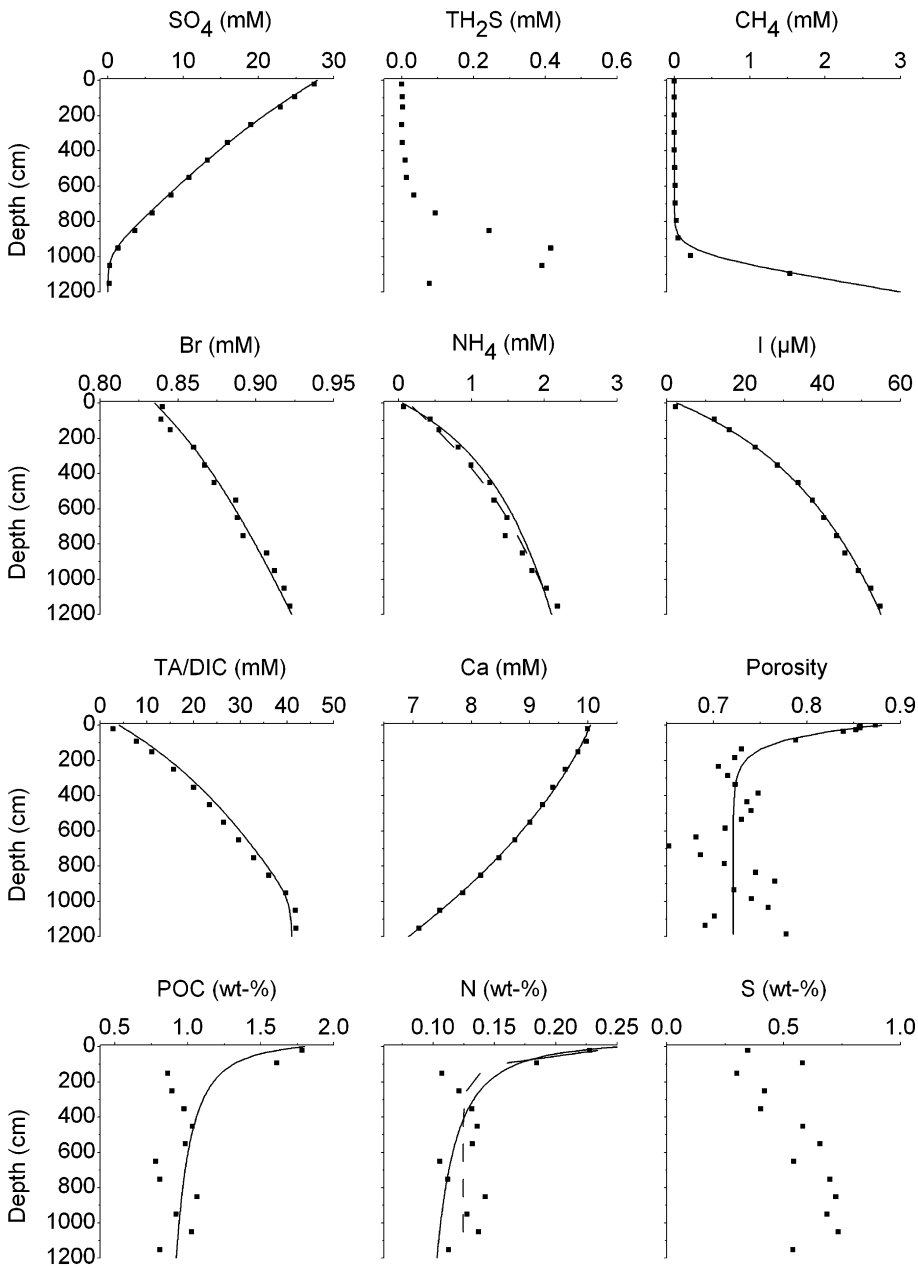

Fig. 4. Data (solid squares) and model results (solid lines) for core SO178 10-6 SL. For further information see legend of Fig. 2.

about 20 cm kyr^{-1}. In the northern core SO178 13-6 KL, the top 10–20 m of the sampled sediments are apparently of Holocene origin indicating sedimentation rates as high as 100–200 cm kyr^{-1} (Dullo et al., 2004). It was, however, difficult to develop a good stratigraphy for the slope sediments because of their low carbonate contents and the varying input of terrestrial materials by ice-rafting, erosion of adjacent shelf deposits, and the Amur River.

Hence, we developed a new approach to derive sedimentation rates from a nitrogen mass balance at steady-state. Sedimentation rates (Table 2) were derived from ammonium, particulate nitrogen, and porosity data as outlined in Section 4. The calculations were done repeatedly using different concentrations measured within the uppermost and lowermost meter of the sediment column. At stations SO178 13-6 KL and SO178 29-2 KL, we considered only the upper 10 and 15 m of the sediment column, respectively, because POC and solid *N* concentrations increased below these depths indicating enhanced POM depositional rates in the underlying sediments. The resulting values depend on the chosen depth level but were found to fall within the error range given in Table 2.

The calculated sedimentation rates confirm both the order of magnitudes and the regional trend previously observed. Sedimentation rates are low in the southern slope area and strongly increase towards the north due to enhanced marine productivity and supply of suspended matter by the Amur River. The good correspondence between

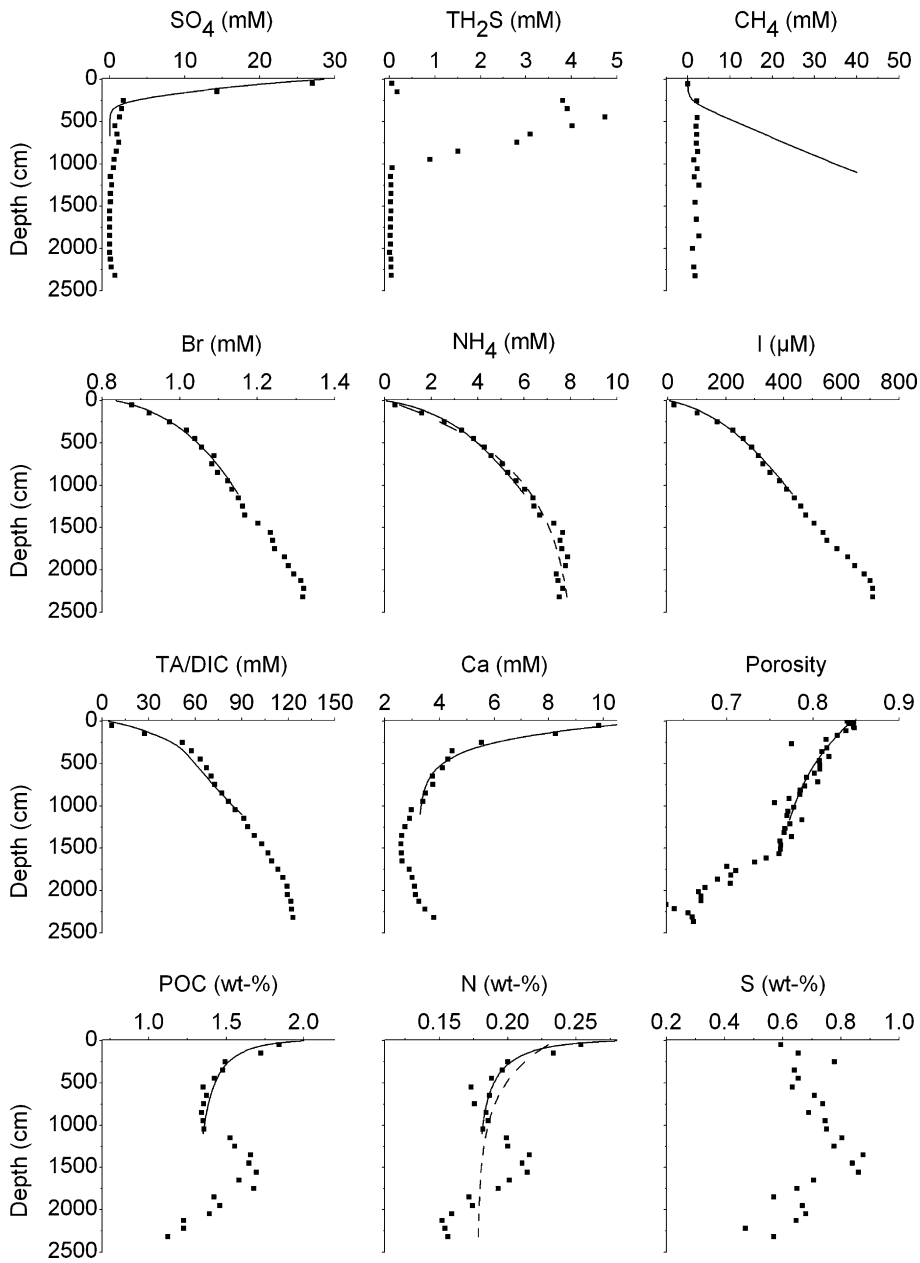

Fig. 5. Data (solid squares) and model results (solid lines) for core SO178 13-6 KL. For further information see legend of Fig. 2.

our results and the previous estimates confirms the validity of the new approach. Sedimentation rates derived from the nitrogen mass balance are particularly well suited for studies on early diagenesis because they provide rates appropriate for steady-state modeling.

5.2. Kinetics of organic matter degradation

Solid phase and pore water data give evidence for high rates of organic matter deposition and degradation in the investigated slope sediments (Figs. 2–7). Concentrations of particulate organic carbon (POC) and total nitrogen (N) increased towards the north due to the enhanced productivity and high sedimentation rates in the northern slope area. A strong south–north gradient in organic matter supply and degradation is also seen in the shoaling of the sulfate penetration depth caused by enhanced rates of microbial sulfate reduction. At the southern stations (SO178 3-4 KL and LV28 2-4 SL) sulfate penetrates to the base of the cores and dissolved methane was not detected. Other electron acceptors such as oxygen, nitrate, manganese and iron oxides were probably consumed within the top few decimeters so that the decrease in dissolved sulfate with depth and the curvature of the sulfate profile reflect the rates of organic matter degradation in the southern cores. In core SO178 10-6 SL, sulfate was depleted at 1050 cm sediment depth (Fig. 4). Below that depth, methane concentrations rapidly increased towards the base of

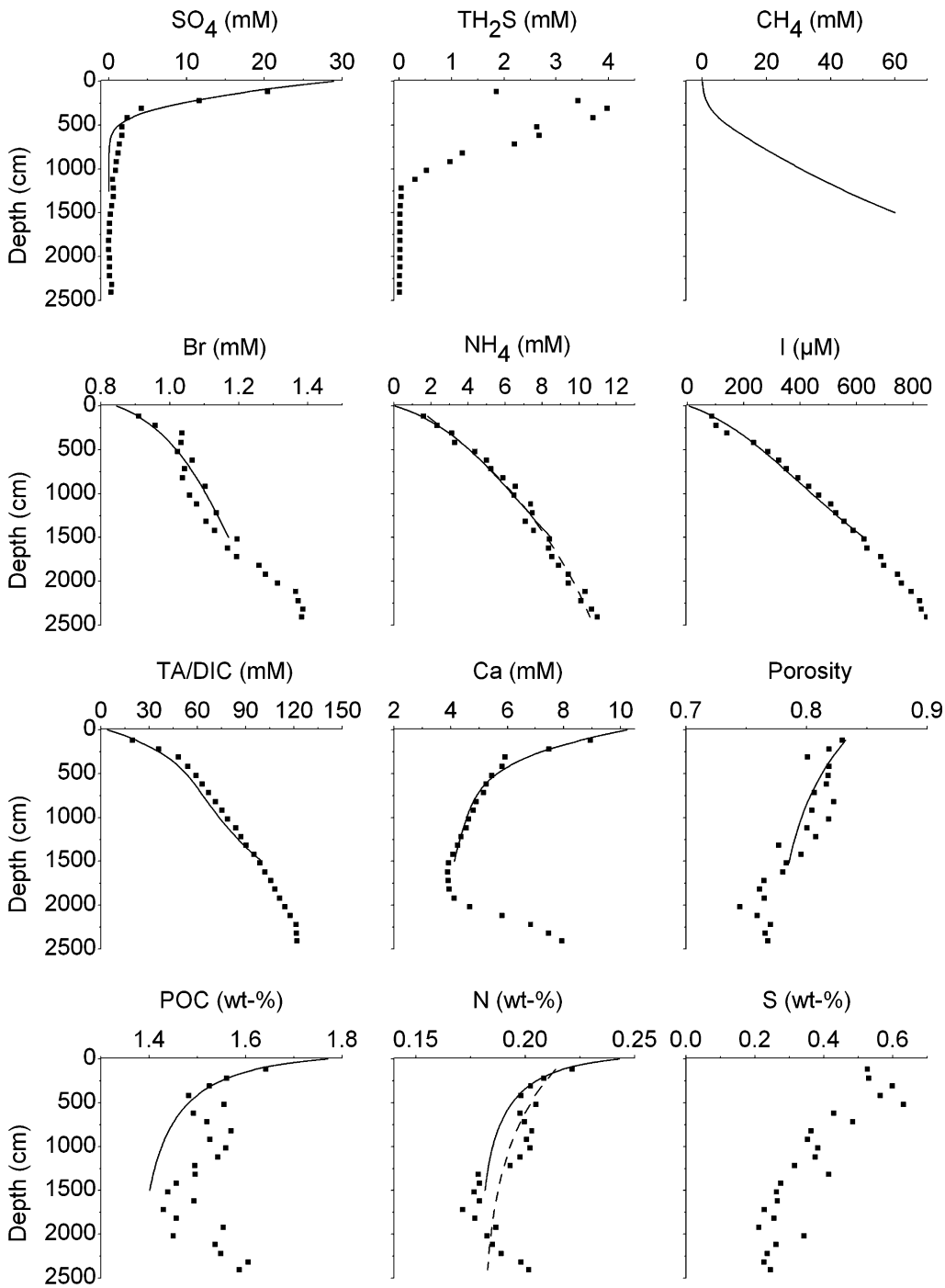

Fig. 6. Data (solid squares) and model results (solid lines) for core SO178 29-2 KL. For further information see legend of Fig. 2.

the core. The AOM layer at around 1000 cm sediment depth is also marked by a strong increase in dissolved sulfide concentration. In the northern cores (SO178 13-6 KL, SO178 29-2 KL, and LV28 20-2 SL) sulfate is already consumed at shallow depths (2–5 m) and methane concentrations start to increase below the sulfate penetration depth.

The initial age of organic matter (a_0) and the constant for the inhibition of organic matter degradation by dissolved inorganic carbon and methane (K_C) were constrained using the decrease in POC and N with sediment depth and the curvature of the dissolved ammonium and sulfate profiles (see Section 4). The initial age needed to calculate the depth and age-dependent kinetic constant k_x (Middelburg, 1989) controls the interfacial gradients in POC and N. Hence, a_0 was varied until the model reproduced the gradients measured in the top meter of the sediment cores. The resulting values (300–3000 yr, Table 2) reflect the age of organic

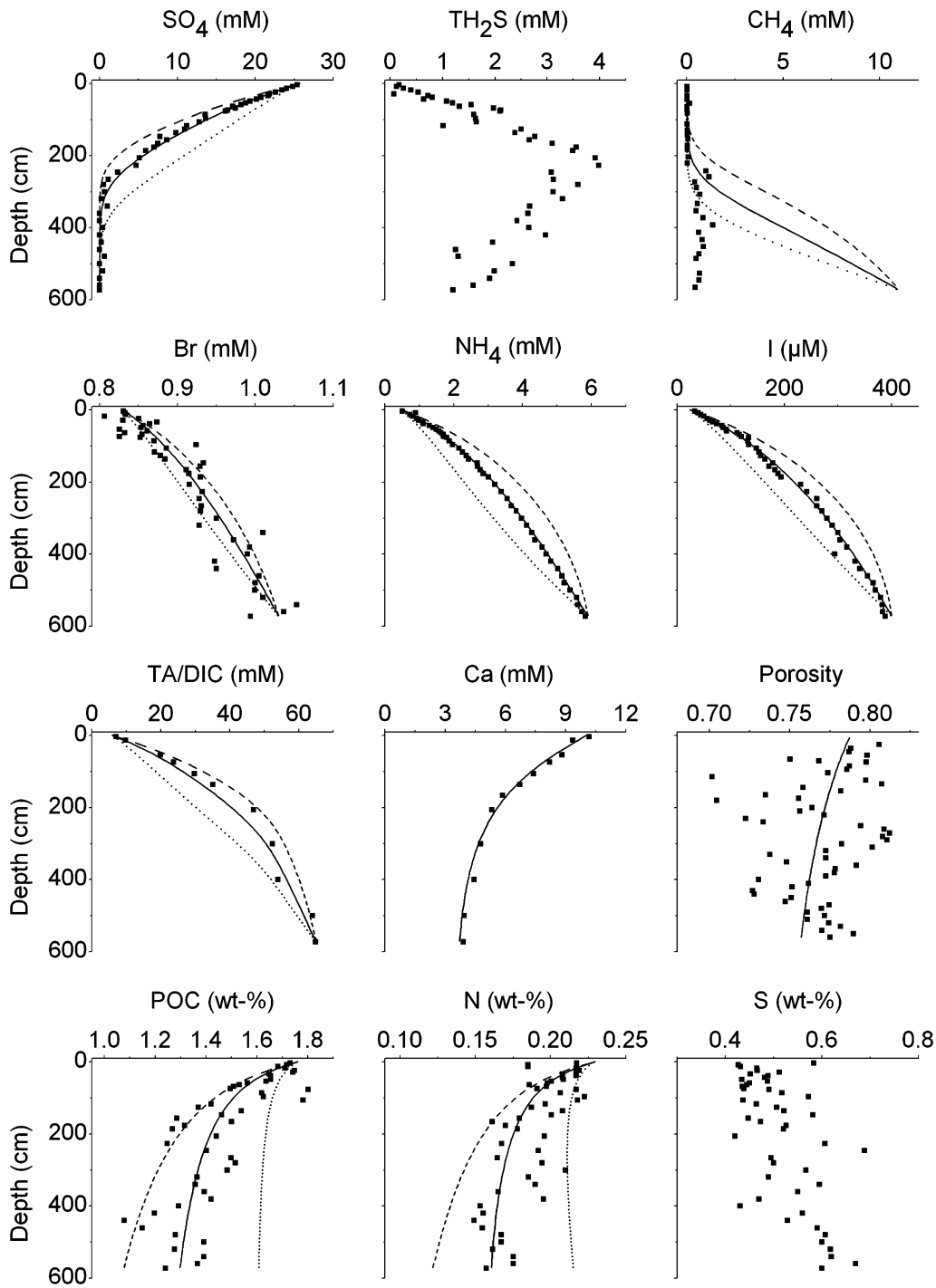

Fig. 7. Data (solid squares) and model results for core LV28 20-2 SL. Solid lines show the best fit to the data attained with an inhibition constant of $K_C = 40$ mM. Dotted lines indicate the results of a model run with $K_C = 4$ mM and broken lines show the model results using $K_C = 400$ mM. For further information see legend of Fig. 2.

matter buried below the bioturbated surface layer which was not resolved by the data and the model. A very large value ($a_0 = 30\ 000$ yr) was used for core SO178 3-4 KL, because the upper decimeters of that particular core were lost during sampling by over-penetration of the coring device. The value of the inhibition constant (K_C) was determined using the curvature of the sulfate and ammonium profiles and the gradients in POC and N in the deeper sediment layers. Sulfate is consumed not only via organic matter degradation but also during AOM. Hence, sulfate data were only applied to constrain organic matter degradation rates in methane-free cores (SO178 3-4 KL and LV28 2-4 SL). Modeled rather than measured concentrations of dissolved inorganic carbon (DIC) and methane were considered in the modeling of

Table 2
Parameter values derived by fitting the model to the data

Parameter (symbol)	SO178 3-4 KAL	LV28 2-4 SL	SO178 10-6 SL	SO178 13-6 KL	SO178 29-2 KL	LV28 20-2 SL	ODP 997
Sedimentation rate (cm kyr^{-1})	10 ± 1	10 ± 5	13 ± 5	93 ± 2	115 ± 5	90 ± 3	22[a]
Initial age of POM (a_0 in yr)	30,000	3000	1000	300	1000	580	2E + 5
Monod constant for the inhibition of POM degradation by DIC and CH_4 (K_C in mM)	30	40	30	40	30	40	35
Monod constant for the inhibition of CH_4 formation by SO_4 (K_{SO_4} in mM)	1.0	1.0	1.0	1.0	1.0	1.0	1.0
Kinetic constant for AOM (k_{AOM} in $cm^3\ yr^{-1}\ mmol^{-1}$)	1.0	1.0	30	10	1.0	20	1.0
Constant for ammonium adsorption (k_{ADS} in $cm^3\ g^{-1}$)	1.7	1.7	1.7	1.7	0.3	1.7	0.6
Atomic N/C ratio for POM degradation (r_N)	16/106	16/106	16/106	16/106	16/106	16/106	16/106
Atomic I/C ratio for POM degradation (r_I)	1.2E-3	1.5E-3	3.5E-3	8.0E-3	8.0E-3	1.0E-2	2.8E-3
Atomic Br/C ratio for POM degradation (r_{Br})	2.0E-3	4.0E-3	3.0E-3	7.0E-3	7.0E-3	4.0E-3	4.0E-3

[a] Sedimentation rate at Site 997 taken from (Davie and Buffett, 2001).

organic matter degradation since most of the dissolved methane and some of the dissolved CO_2 were lost during sampling due to the decrease in pressure upon core retrieval. Methane concentrations at the core base were varied until the resulting AOM rates produced sulfate penetration depths consistent with the data. DIC concentrations at the core base were set according to the measured values of total alkalinity. The resulting K_C values fall into a narrow range of 30–40 mM indicating that the kinetic rate law defined in Eq. 3 is well suited to describe the inhibiting effect of DIC and methane on organic matter degradation over a large range of sedimentary environments (Table 2).

The sensitivity of the model results with respect to the value of the inhibition constant (K_C) is shown in Fig. 7. The best fit to the data was obtained using $K_C = 40$ mM. Two additional model runs were performed applying K_C values of 4 mM (dotted lines) and 400 mM (broken lines). The other model parameters were not changed in these model runs but maintained at the values listed in Table 2. Organic matter degradation rates were diminished applying the reduced K_C value because the degradation rates were now suppressed already at low concentrations of DIC and methane. Consequently, the concentrations of POC and N increased at the core base while the concentrations of dissolved metabolites were substantially reduced. A large K_C value decreased the solid phase concentrations at the core base and substantially increased the curvature of the metabolite profiles. Not only the ammonium pore water data but also the profiles of DIC, bromide and iodide were strongly affected by the variation of the inhibition constant. The well constrained iodide data thus give further evidence for the inhibition of organic matter degradation. The strong sensitivity of the model results with respect to the value of the inhibition constant and the good fit obtained in the standard run ($K_C = 40$ mM) demonstrate that the data set used in this study can be explored to both trace the inhibition of organic matter degradation by metabolites and constrain the inhibition constant.

In the following, the new kinetic model is compared with previous models of organic matter degradation. Multi-G models have been commonly used to simulate the degradation of organic matter in marine sediments (Westrich and Berner, 1984; Boudreau, 1996b; Luff et al., 2000). In these models, the organic matter is separated into several fractions with different reactivity. Here, a 2-G model is tested where the organic matter is assumed to be composed of a labile (G1) and a more refractory fraction (G2). The rate of organic carbon degradation is calculated as:

$$R_{POC} = k_1 \cdot G_1 + k_2 \cdot G_2, \tag{9}$$

and the particulate organic carbon concentration is defined as:

$$POC = f_{POC} \cdot G_1 + (1 - f_{POC}) \cdot G_2. \tag{10}$$

The parameters of the kinetic model were constrained by fitting the model to the pore water and solid phase data of core LV28 2-4 SL. The best fit was obtained applying $k_1 = 3 \times 10^{-4}\ yr^{-1}$ as kinetic constant for the labile fraction and $k_2 = 5 \times 10^{-6}\ yr^{-1}$ for the refractory fraction assuming that 20% of the total organic carbon occur in the labile form ($f_{POC} = 0.2$).

The other commonly used type of kinetic rate law considers organic matter to be composed of a very large number of different molecules each having its own reactivity. The first and most popular version is Middelburg's age-dependent model:

$$R_{POC} = k_x \cdot POC = 0.16 \cdot \left(a_0 + \frac{x}{w}\right)^{-0.95} \cdot POC. \tag{11}$$

It predicts that the reactivity of organic matter decreases continuously with age and sediment depth and serves as base for the new kinetic model presented in this paper. Both traditional models assume that degradation rates are not affected by the pore water composition whereas the new kinetic rate law presented in this paper predicts that rates are suppressed by the accumulation of dissolved metabolites.

Fig. 8 compares the results obtained with 2-G kinetics, the age-dependent approach and the new rate law. The fully anoxic core LV28 20-2 SL was used for these simulations because this core was sampled with the highest depth resolution. The parameter values applied in the previous

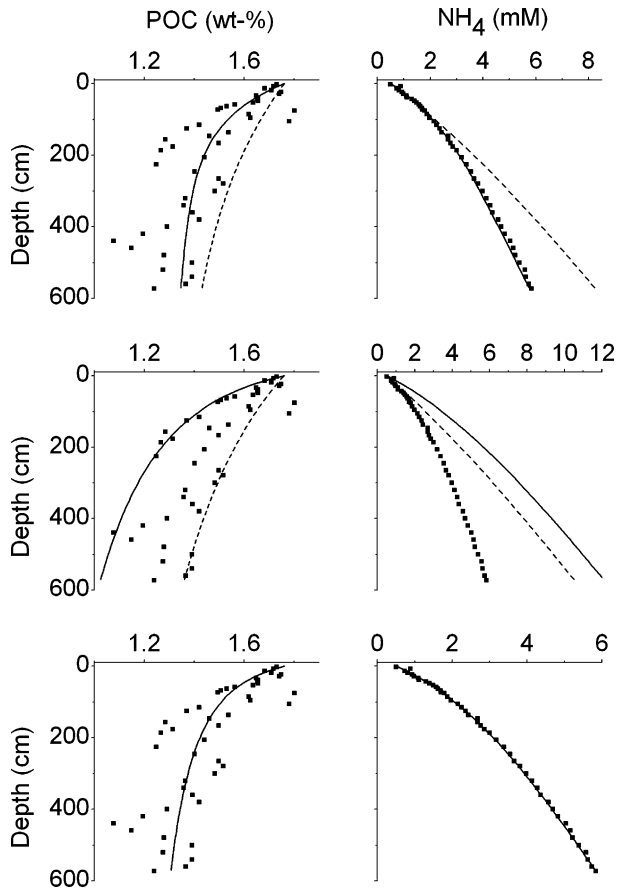

Fig. 8. Data (solid squares) and model results for core LV28 20-2 SL. The upper two panels show the results obtained with the 2-G model. Solid lines indicate the best fit produced with $k_1 = 1 \times 10^{-3}\,\mathrm{yr}^{-1}$ and $k_2 = 8 \times 10^{-6}\,\mathrm{yr}^{-1}$ whereas broken lines were calculated applying the rate constants derived from core LV28 2-4 SL ($k_1 = 3 \times 10^{-4}\,\mathrm{yr}^{-1}$ and $k_2 = 5 \times 10^{-6}\,\mathrm{yr}^{-1}$). The middle panels show results produced with the age-dependent model (solid line: $a_0 = 580$ yr; broken line $a_0 = 2000$ yr) while the bottom panels depict the results obtained with the new rate law.

standard model run (Table 2) were also used in these addition model simulations. Constant gradients rather than prescribed concentrations were, however, applied at the lower boundary to better evaluate the prognostic capacity of the different kinetic models. In other words, the concentration gradients of dissolved species in the last interval of the model column (n) were now set to the value calculated for the overlying depth interval ($n - 1$).

$$\frac{\delta C}{\delta x}(n) = \frac{\delta C}{\delta x}(n-1). \tag{12}$$

Applying the kinetic parameters derived from core LV28 2-4 SL to core LV28 20-2 SL, the 2-G model was not able to reproduce the data (Fig. 8). A good fit was, however, obtained when the kinetic constants were adjusted to $k_1 = 1 \times 10^{-3}\,\mathrm{yr}^{-1}$ and $k_2 = 8 \times 10^{-6}\,\mathrm{yr}^{-1}$. The organic matter at the northern site LV28 20-2 SL was, thus, more reactive than the sedimentary organic matter retrieved at the southern station LV28 2-4 SL. This significant difference in reactivity probably reflects the large contrast in sedimentation rate between the two sites. At the southern location sedimentation was low (10 cm kyr^{-1}) whereas the northern station receives more terrigenous sediments from the adjacent Amur River inducing a much higher sedimentation rate (90 cm kyr^{-1}). The age of sedimentary organic matter at a given depth level, therefore, increases towards the south. Since, the reactivity of organic matter decreases with sediment age, the kinetic constants are lower at the southern station. Several authors recognized that the reactivity of organic matter during anaerobic degradation depends on sedimentation rate (Boudreau, 1997). Thus, Tromp et al. (1995) provided an empirical equation relating the kinetic constant for POC degradation via sulfate reduction to sedimentation rate. This equation correctly predicts that the reactivity of organic matter increases with sedimentation rate but does not consider the decrease in reactivity with sediment depth observed in our data. The 2-G model applied here mimics the decrease in reactivity with sediment depth. It proved to be a useful tool to fit pore water and solid phase data. The best-fit values for the kinetic parameters differed, however, considerably among individual cores. To this date, no a priori method is available for predicting the rate constants of organic matter degradation in anoxic sediments over a wide range of sedimentary environments and sediment depths. The available multi-G models are, hence, not suitable for prognostic modeling.

Degradation rates predicted by the age-dependent model without inhibition term were too high over the deeper part of the sediment column (Fig. 8). An increase in the initial age a_0 from the standard value (580 yr) to 2000 yr reduced the overall degradation rates but could not mimic the strong decrease in degradation with sediment depth observed in the data. The original model was mainly calibrated using short sediment cores with low dissolved metabolite concentrations (Middelburg, 1989). The data and modeling presented in this paper indicate that organic matter is more slowly degraded in anoxic sediments with high metabolite concentrations than predicted by Middelburg's model for a given sediment age.

The new rate law introduced in this paper produced an excellent fit to the data also with the constant gradient condition applied at the lower boundary (Fig. 8). The good fit obtained in the previous standard simulation with a constant ammonium concentration prescribed at the base of the core is, thus, not a result of the lower boundary condition but rather reflects the inherent reactivity of organic matter in core LV28 20-2 SL. In contrast to the previous kinetic models, the new model correctly predicts organic matter degradation rates in anoxic slope deposits over a wide range of sedimentation rates and sediment depths.

5.3. Bromine and iodine cycling

Dissolved bromide and iodide concentrations in the pore water increased with sediment depth and towards the north (Figs. 2–7). Both halogens are released into the

pore water by the microbial degradation of POM. The pore fluids were significantly enriched in dissolved bromide. Bromide release rates were calculated from the POC degradation rates applying Br/POC ratios (r_{Br}) that produced a good fit the pore water profiles. The resulting values ($r_{Br} = 2–7 \times 10^{-3}$; Table 2) were on average higher than the plankton ratio (2.2×10^{-3}). Previous work showed that atomic Br/POC ratios in surface sediments ($0.3–2 \times 10^{-3}$) are lower than the plankton ratio and decrease with depth implying a preferential degradation of Br-bearing organic matter (Martin et al., 1993). This preferential release of bromide is confirmed by our data.

Extremely high iodide concentrations of more than 0.8 mM were found at the base of core SO178 29-2 KL (Fig. 6). Comparable concentrations were previously found in sediment cores retrieved by deep-sea drilling albeit at much larger sediment depth (Martin et al., 1993; Egeberg and Dickens, 1999). The high iodide concentrations reflect the enormous burial flux of organic matter in the northern slope region produced by a combination of very high marine productivity and intense terrigenous sedimentation. Atomic ratios between the release of iodide and inorganic carbon (r_I) were determined by fitting the model to the data. They were found to increase towards the north by one order of magnitude (Table 2). All ratios were significantly higher than the atomic I/POC ratio of plankton (1.4×10^{-4}; Elderfield and Truesdale, 1980) indicating additional iodine sources or the preferential degradation of iodine-bearing organic compounds. Previous studies showed that iodide released at depth diffuses to the sediment surface to be taken-up at the oxic interface by microbially mediated redox processes (Kennedy and Elderfield, 1987). Oxic surface sediments attain very high I/POC ratios in the solid phase (up to 3×10^{-3}) due to the uptake of iodide from the pore water (Kennedy and Elderfield, 1987). Moreover, previous pore water data suggest that I is preferentially released into solution during microbial degradation processes. Hence, I/POC regeneration ratios of 0.1–34×10^{-3} were found in oxic to suboxic marine surface sediments (Kennedy and Elderfield, 1987). The values derived for our anoxic slope cores ($1–10 \times 10^{-3}$) fall into this range (Table 2). They indicate that the preferential release of iodide is not limited to the more oxidizing surface sediments but occurs also in deeper anoxic layers. The regular increase in these ratios towards the more productive northern slope indicates that high regeneration ratios are maintained in strongly anoxic sediments receiving a large flux of marine organic matter.

5.4. Sulfur cycling

Dissolved sulfate and sulfide profiles and concentrations of total sulfur in the solid phase were used to characterize the turnover of sulfur in the studied anoxic sediments (Figs. 2–7). Among these parameters, dissolved sulfate is most suitable for the modeling since sulfide is partly lost during core retrieval and pore water separation while pyrite formation may start already within the bioturbated surface layer not resolved by the model (Fossing et al., 2000). Solid phase sulfur concentrations were indeed high in the uppermost sediment samples (Figs. 2–7) reflecting the formation of pyrite in reactive surface sediments. Dissolved sulfide profiles showed distinct maxima in the sulfate-methane transition zone where sulfide was rapidly produced by AOM. In contrast, the dissolved sulfide concentrations were low and close to the detection limit in methane-free sediments indicating that sulfide produced during sulfate reduction via organic matter degradation was almost completely removed from the pore water by the formation of pyrite and other authigenic sulfur phases.

The benthic sulfate fluxes at the sediment surface (Table 3) ranging in between 10 and 200 mmol m^{-2} yr^{-1} are a measure for the total sulfate consumption in sediments underlying the bioturbated surface layer. These fluxes increase towards the north due to enhanced rates of organic matter sedimentation. They are similar to those reported for other reactive continental margins such as the western Argentine Basin (Hensen et al., 2003), and the Black Sea (Jørgensen et al., 2001). The benthic fluxes are driven by sulfate reduction via organic matter

Table 3
Depth-integrated turnover rates and fluxes (in mmol m^{-2} yr^{-1}) calculated in the model and length of the sediment column considered in the modeling (in m)

Rate/flux	SO178 3-4 KAL	LV28 2-4 SL	SO178 10-6 SL	SO178 13-6 KL	SO178 29-2 KL	LV28 20-2 SL	ODP 997
Length of model column	10	6	12	11	15	5.7	451
POC degradation	12.7	39.5	68.3	325	207	233	27.2
PON degradation	1.91	5.96	10.3	49.1	31.3	35.2	4.11
POI degradation	0.015	0.059	0.239	2.60	1.66	2.33	0.076
POBr degradation	0.025	0.158	0.205	2.28	1.45	0.934	0.108
SO_4 reduction via POC degr.	6.08	19.0	31.6	122	76.9	104	2.76
Methane formation	0.25	0.76	2.50	40.4	26.7	13.0	10.8
AOM	0.205	0.467	16.1	78.5	59.0	45.4	10.5
Ammonium adsorption	0.071	0.101	0.319	6.00	1.68	5.48	3.00
$CaCO_3$ precipitation	−0.48	3.38	−0.54	29.6	15.5	21.6	n.d.
Benthic SO_4 flux	10.4	27.9	47.9	201	136	149	13.4
POC burial	36.2	58.8	69.5	662	772	641	303
N burial	4.06	4.00	6.67	76.0	85.7	68.1	37.7

degradation and AOM. Depth-integrated rates of these processes increased towards the north (Table 3). In the three northern cores, sulfate was consumed via organic matter degradation at a mean rate of $101 \pm 23\,\mathrm{mmol\,m^{-2}\,yr^{-1}}$ while the average AOM rate was $61 \pm 17\,\mathrm{mmol\,m^{-2}\,yr^{-1}}$. Hence, about 40% of sulfate was consumed by AOM in the northern slope area. The fraction of sulfate being consumed by AOM rather than organic matter degradation seems to be highly variable at different continental margin sites. Thus, Fossing et al. (2000) and Jørgensen et al. (2001) performed sulfate reduction rate measurements in continental margin sediments off Namibia and in the Black Sea showing that only a minor portion of the depth-integrated sulfate consumption is due to AOM. In contrast, Niewöhner et al. (1998) observed linear sulfate gradients in surface sediments at the U.S. North Atlantic and Namibia continental margins overlying major gas hydrate deposits and concluded that sulfate reduction is almost completely driven by AOM at these sites. The significant curvature in the sulfate, ammonium, bromide and iodide profiles observed in the sediments off Sakhalin (Figs. 2–7) demonstrates, however, that organic matter degradation contributes significantly to the overall sulfate reduction in these slope deposits.

5.5. $CaCO_3$ turnover

Solid phase concentrations of $CaCO_3$ were low over the entire slope area ranging in between 0 and 2 wt% with a mean value of 0.5 wt% in the sampled slope sediments (data not shown). Pore water profiles of dissolved Ca indicate, however, that both carbonate dissolution and precipitation may occur in anoxic slope deposits off Sakhalin (Figs. 2–7). In the southernmost core (SO178 3-4 KAL) Ca concentrations increased with depth suggesting a depth integrated $CaCO_3$ dissolution rate of $0.48\,\mathrm{mmol\,m^{-2}\,yr^{-1}}$ (Table 3). Core LV28 2-4 SL experienced $CaCO_3$ precipitation over the entire core length (Fig. 3) while the dissolved Ca profile in core SO178 10-6 SL suggests $CaCO_3$ dissolution in the upper layers and $CaCO_3$ precipitation at the base of the core (Fig. 4). The northern cores (Figs. 5–7) showed signs of $CaCO_3$ precipitation in the upper ~15 m followed by $CaCO_3$ dissolution in the deeper layers.

Carbonate dissolution/precipitation are manly driven by the release of CO_2 and HCO_3 during the anaerobic degradation of organic matter and the oxidation of methane. During degradation of organic matter (here represented as simple carbohydrate $C(H_2O)$) via sulfate reduction both CO_2 and HCO_3^- are released while sulfide is fixed in pyrite:

$$7/2C(H_2O) + Fe^{2+} + 2SO_4^{2-} \Rightarrow 2HCO_3^- + 3/2CO_2 + FeS_2 + 5/2H_2O$$

Fe^{2+} may either originate from the microbial reduction of iron oxides or iron-bearing clay minerals and carbonates. Models show that $CaCO_3$ is dissolved at low rates and during the initial phase of sulfate reduction while $CaCO_3$ precipitation prevails at high rates of sulfate reduction via organic matter degradation (Boudreau and Canfield, 1993). These model predictions are confirmed by some of our data showing $CaCO_3$ dissolution at low sulfate reduction rates (core SO178 3-4 KL) and in the upper section of the sulfate reduction zone (core SO178 10-6 SL).

During AOM, carbonate alkalinity is generated and bisulfide accumulates in the pore water:

$$CH_4 + SO_4^{2-} \Rightarrow HCO_3^- + HS^- + H_2O$$

Hence, AOM induces $CaCO_3$ precipitation in marine sediments (Wallmann et al., 1997; Luff and Wallmann, 2003). The pore water data clearly show that Ca concentrations always decrease towards the base of the sulfate-bearing zone confirming that $CaCO_3$ is precipitated during the anaerobic oxidation of methane. The average depth-integrated rate of carbonate precipitation in the three northern cores is $22 \pm 7\,\mathrm{mmol\,m^{-2}\,yr^{-1}}$ while the AOM rate amounts to $61 \pm 17\,\mathrm{mmol\,m^{-2}\,yr^{-1}}$ in these cores (Table 3). The data hence suggest that one third of the carbonate alkalinity generated via AOM is removed from the pore water via authigenic $CaCO_3$ precipitation. A similar proportion was previously found at active cold vent sites where methane-charged fluids ascend to the sediment surface (Luff et al., 2004).

In the underlying zone, methane and CO_2 are generated during the degradation of organic matter:

$$2C(H_2O) \Rightarrow CO_2 + CH_4$$

Carbonates should hence be dissolved in the methanogenic zone as indeed suggested by the increase in dissolved Ca towards the base of cores SO178 13-6 KL and SO178 29-2 KL (Figs. 5,6). We observed however a remarkable increase in total alkalinity within the methanogenic zone which is probably not driven by the degradation of organic matter or the dissolution of $CaCO_3$ but rather by the chemical weathering of silicate phases as previously observed in other anoxic marine sediments (Aloisi et al., 2004; Maher et al., 2004).

5.6. Organic matter degradation and gas hydrate formation at Blake Ridge

Gas hydrate formation at Blake Ridge, a large drift deposit located at the passive continental margin of the south-eastern United States, has been studied in detail during ODP Leg 164 (Dickens et al., 1997). According to the ODP data, hydrates occupy in between 4% and 7% of pore space in these sediments between 186 and 451 mbsf. The excellent set of pore water data retrieved from Site 997 has been used repeatedly to constrain the velocity of upward fluid flow, rates of methane oxidation and gas hydrate formation and the hydrate distribution in these deposits. Egeberg and Dickens (1999) used the curvature of the bromide and iodide pore water profiles and the

dissolved Br/I ratio to constrain the velocity of upward fluid flow as 0.2 mm yr^{-1}. This values should, however, be considered as a maximum estimate since pore water burial and the in situ production of halogens from organic matter degradation processes were neglected by the authors. They further used the dissolved chloride profiles to derive rates of gas hydrate formation. These rates were not related to the organic carbon data and the concentrations of dissolved metabolites in pore fluids but were prescribed as a rather arbitrary source function satisfying the chloride observations. Davie and Buffett published a series of papers on the rates and mechanisms of hydrate formation at Black Ridge (Davie and Buffett, 2001, 2003a,b). They finally concluded that the Blake Ridge observations (dissolved sulfate and chloride profiles, gas hydrate concentrations) can be explained by microbial methane production within the lower part of the HZS combined with an inflow of fluids (0.23 mm/yr) transporting methane and acetate from the deep underground into the HSZ (Davie and Buffett, 2003b). Since an unreasonable large fraction of sedimentary organic matter has to be degraded to produce the observed hydrate accumulation, inflowing acetate rather than POC might be the main substrate for methane production at this site (B. Buffett, pers. communication).

We used Site 997 to test our new kinetic model on a well studied reference location and to calculate rates of methane production and hydrate precipitation within the HSZ. In contrast to previous modeling studies at Blake Ridge, we evaluate the entire biogeochemical data set including concentration profiles of dissolved metabolites (ammonium, bromide, and iodide), dissolved sulfate, particulate organic carbon, and total nitrogen (Fig. 9). Based on this comprehensive approach, the gas hydrate formation through organic matter degradation was quantified much more reliably than in previous model studies. The model was modified to consider the specific conditions at Blake Ridge (Appendix B). Thus, organic matter concentrations measured in surface sediments are significantly lower than those observed at large sediment depths (see POC and *N* in Fig. 9). This important observation strongly suggests a decrease in organic matter deposition over time. To mimic this non-steady-state situation, we applied a time-dependent POC concentration at the top of the model column. Interfacial POC concentrations were kept constant at a value of 1.6 wt% over a period of 5 Myr and were forced to decrease linearly over the last 0.7 Myr of the model period to a modern value of 0.65 wt%. Sedimentation rates and temperature gradients were taken from Davie and Buffett (2001) while pressures were calculated from water and sediment depths assuming hydrostatic conditions. Moreover, hydrate precipitation, upward fluid flow, and the temperature effect on molecular diffusion were included in the extended model version applied to Blake Ridge (Appendix B).

The best fit to the data was obtained with the set of parameter values listed in Table 2 and an interstitial fluid flow velocity of 0.12 mm yr^{-1} at the sediment surface. The initial age of the decaying organic matter was set to a high value since the almost linear sulfate profiles at Blake Ridge suggest low rates of organic matter degradation in surface sediments. Black Ridge is a sediment drift that consists of hemipelagic silt and clay-rich contourite deposits originating from northern continental slope areas (Paull et al., 2000). Late Quaternary sedimentation rates are about one order of magnitude lower than the average sedimentation rate applied in the modeling (Paull et al., 2000). The high initial age may thus reflect the slow deposition of reworked old organic matter at the sediment surface. The good fit to the pore water and sediment data (Fig. 9) shows that the kinetic model can be used to constrain rates of organic matter degradation and microbial methane formation not only in surface sediments of the Sakhalin slope area but also over the entire HSZ of Blake Ridge and presumably other continental margin sites.

Rates of biogenic methane production decreased over time due to the diminished deposition of organic carbon at the top of the model column (Fig. 10). The rate profile at 0.7 Myr represents the steady-state attained after the interfacial POC concentration was maintained at a constant value of 1.6 wt% over a period of 5 Myr. The subsequent decrease in the interfacial POC values induced a significant drop in methane production over the top 200 m of the sediment column. The rate maximum was shifted from 22 m at 0.7 Myr to 28 m sediment depth for the modern situation since the reduced methane production allowed for a deeper penetration of dissolved sulfate. Methane production was suppressed in the sulfate-bearing surface layer and decreased below the rate maximum due to the low reactivity of old organic matter and the increasing concentrations of DIC and methane. The shallow rate maximum is a result of the new kinetic law applied in the model. It induces a significant methane production at shallow depth which does not directly contribute to the formation of hydrates since methane is lost by rapid diffusion into the adjacent sulfate-bearing layer where methane is consumed by anaerobic oxidation.

Hydrate concentrations calculated in the model are at least one order of magnitude lower than the values obtained during ODP drilling. This significant difference suggests that most of the hydrate-bound methane is neither formed by in situ organic matter degradation nor transported to the HSZ by the ascent of methane-charged fluids. Gas bubbles ascending from deep sediments were recently found to deliver abundant methane to the HSZ at Hydrate Ridge (Torres et al., 2004). A similar process may also take place at Blake Ridge. Thus Gorman et al. (2002) presented seismic data suggesting that gas bubbles from below the HSZ migrate upwards into the HSZ at Blake Ridge. Flemings et al. (2003) showed that lithostatic gas pressures prevail in the interconnected gas column formed below the HSZ at Site 997. They propose that this over-pressured gas reservoir may exceed the strength of the sediment above driving fractures that vent methane gas into the HSZ. Our model analysis supports this view and implies

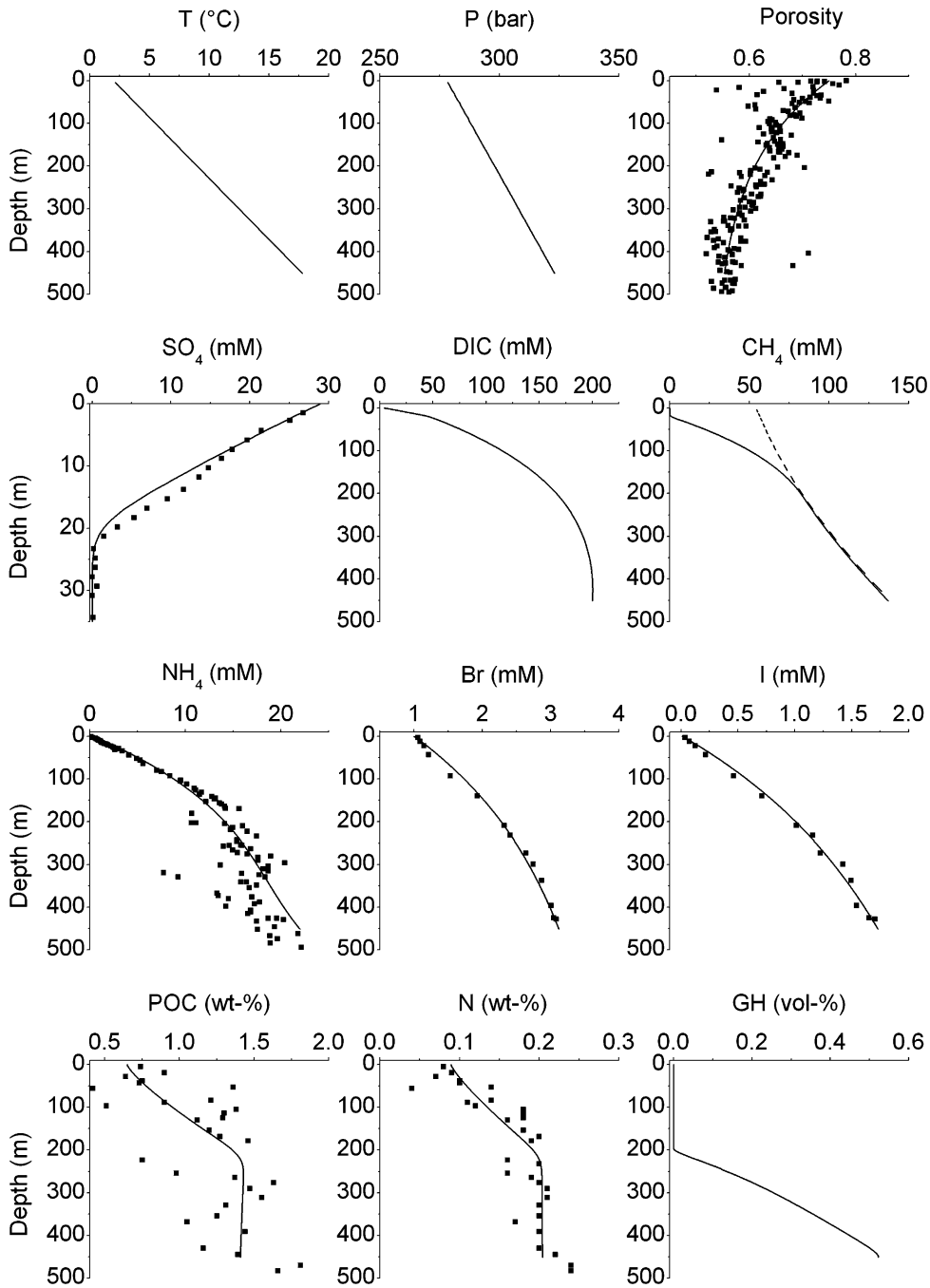

Fig. 9. Data (solid squares) and model results (solid lines) for ODP Site 997. Top row: Temperature (T), pressure (P), and porosity. Second row: Concentrations of dissolved sulfate (SO_4, note that only the upper 35 m of the sediment column are plotted since sulfate is depleted in deeper sediment layers), concentrations of dissolved inorganic carbon (DIC), dissolved methane (CH_4, solid line: calculated concentrations, broken line: solubility of gas hydrates). Third row: Dissolved ammonium (NH_4), bromide (Br), and iodide (I). Bottom row: Concentrations of particulate organic carbon (POC), total nitrogen (N = organic N + adsorbed NH_4) and gas hydrates (GH, given in % of pore volume filled by hydrate).

that most of the Blake Ridge hydrates are formed by bubble ascent.

5.7. Gas hydrate formation in Sakhalin slope sediments

The new kinetic model was applied to quantify rates of gas hydrate formation via organic matter degradation along the Sakhalin slope. Modeling was performed for slope sediments located at a constant water depth of 700 m. Lüdmann and Wong (2003) estimated an average geothermal gradient of 33 ± 9 °C km^{-1} from seismic BSR observations in the northern slope area. Considering the ambient bottom water temperature (2 °C) and hydrostatic loading, this estimate implies that the thermodynamically controlled transition from pure hydrate to free gas should occur at a sediment depth of 300 m (Tishchenko et al.,

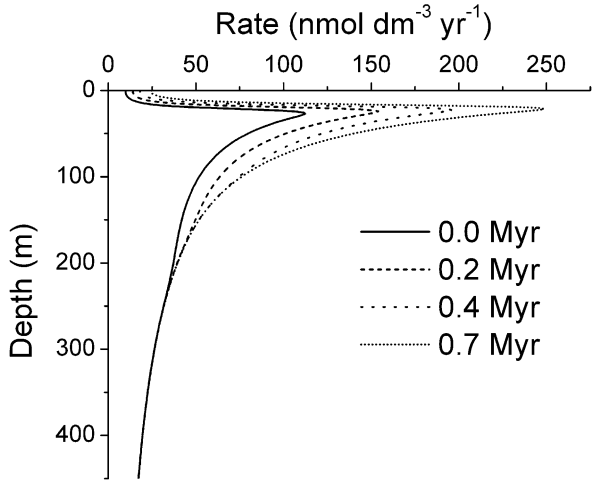

Fig. 10. Rates of biogenic methane production in Blake Ridge sediments as calculated in the non-steady-state model. Rate profiles are plotted for four different times. The highest values were attained at 0.7 Myr before present after a constant POC concentration of 1.6 wt% was applied over a period of 5 Myr at the top of the model column. Subsequently the interfacial POC value was linearly reduced to a modern value of 0.65 wt%. In response to this model forcing rates of methane production significantly decreased over time.

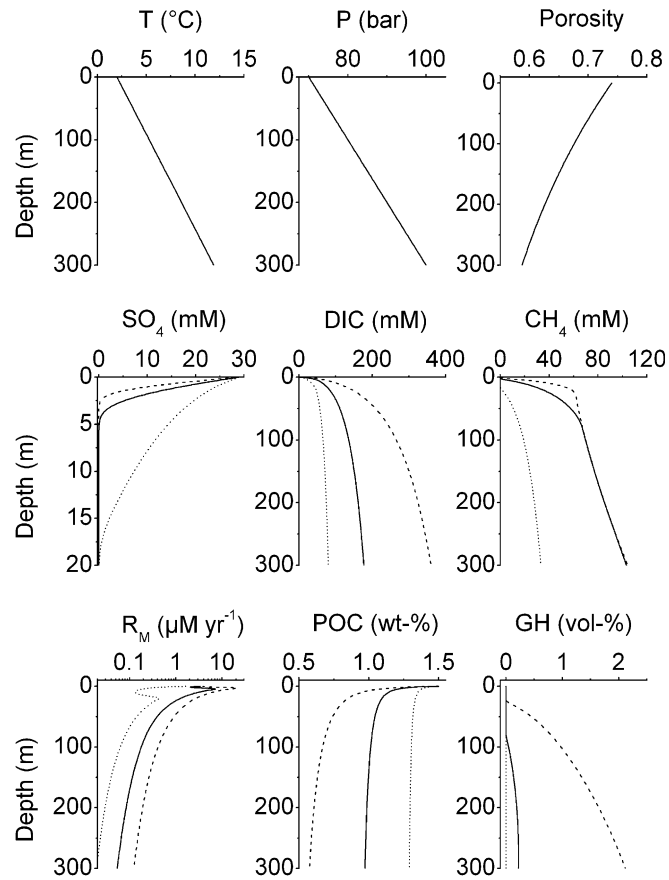

Fig. 11. Inhibition of gas hydrate formation in Sakhalin slope sediments. Top row: Temperature (T), pressure (P), and porosity. Second row: Concentrations of dissolved sulfate (SO_4, note that only the upper 20 m of the sediment column are plotted since sulfate is depleted in deeper sediment layers), concentrations of dissolved inorganic carbon (DIC), dissolved methane (CH_4). Third row: Rate of methane formation (R_M, note the logarithmic scale), concentrations of particulate organic carbon (POC) and gas hydrates (GH, given in % of pore volume filled by hydrate). Dotted line: $K_C = 3.5$ mM; solid line $K_C = 35$ mM (standard value); broken line: $K_C = 350$ mM.

2005). The model was hence run for a column extending from the sediment surface to a depth of 300 m covering the entire HSZ. The porosity profile was adjusted to fit ODP observations in diatomaceous clayey silt sediments as summarized in Einsele (2000). The inhibition constant was varied over two orders of magnitude to investigate the effect of metabolite inhibition on gas hydrate formation while the sedimentation rate was varied in between 10 and 100 cm kyr^{-1} in order to mimic the south-north gradient in sediment accumulation. Equations and parameter values applied in the modeling are presented in Appendix B.

A first set of steady-state models was run applying a sedimentation rate of 50 cm kyr^{-1}, an interfacial POC concentration of 1.5 wt% and an initial age of 1000 yr. No external pore water flow was prescribed so that solutes were transported via diffusion, burial and compaction, only. A constant gradient condition was applied at the lower boundary and the inhibition constant (K_C) was varied in between 3.5 and 350 mM (Fig. 11). Applying a high K_C value of 350 mM, concentrations of dissolved methane and DIC have only a small effect on organic matter degradation. Consequently, POC concentrations decrease rapidly with depth and considerable amounts of gas hydrate accumulate in the model column. Hydrate concentrations increase with depth and reach a maximum value of 2.1 vol% at the base of the core. Applying a small K_C value of 3.5 mM, organic matter degradation is already suppressed at low metabolite concentrations. Methane production and hydrate formation are, thus, inhibited and dissolved methane is under-saturated with respect to gas hydrate over the entire model column. Using the previously derived K_C value of 35 mM, hydrates start to accumulate below a sediment depth of 78 m and reach a maximum concentration of only 0.23 vol% at 300 m depth. The strong sensitivity of hydrate accumulation towards the K_C value clearly demonstrates that the amount of gas hydrate formed within the hydrate stability zone is regulated by the extent of metabolite inhibition.

The effect of sedimentation rate on hydrate accumulation was tested in a second set of model runs. The inhibition constant was set to the value previously derived by the systematic evaluation of pore water and sediment data from the Sakhalin slope ($K_C = 35$ mM) and the sedimentation rate was varied in between 10 and 100 cm kyr^{-1} applying the same set of parameter values as in the previous sensitivity test. Both, the thickness of the hydrate-bearing zone and the average hydrate concentration in that zone strongly increase with sedimentation rate (Fig. 12). Below a sedimentation rate of 30 cm kyr^{-1}, methane production rates are too low to induce hydrate formation. The steady increase in hydrate accumulation with sedimentation rate is caused by the age-dependent

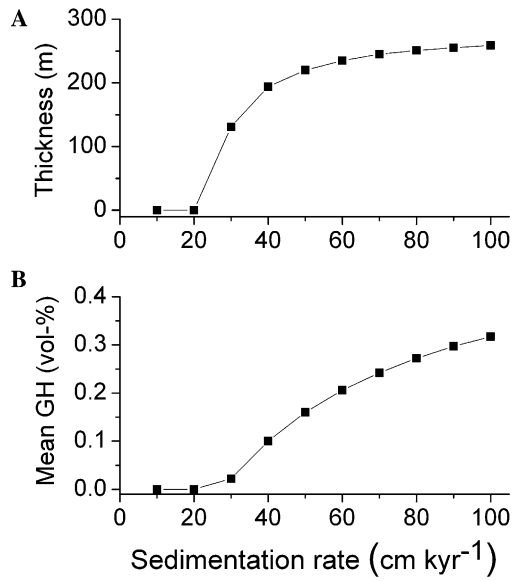

Fig. 12. Gas hydrate formation in Sakhalin slope sediments as a function of sedimentation rate. (A) Thickness of the hydrate-bearing layer (hydrate concentration >0.001 vol%). (B) Mean gas hydrate concentration in the hydrate-bearing layer (given in % of pore volume filled by hydrate).

reactivity of organic matter. In rapidly accumulating sediments, young organic matter is buried to large sediment depths so that abundant methane is formed also in deep layers where the diffusive loss of methane is minimized by low methane gradients.

The model predicts that hydrates do not form along the southern slope of Sakhalin where sedimentation is low whereas hydrates should accumulate in the northern slope area. Lüdmann and Wong (2003) detected a strong BSR in the entire northern slope region and an overlying broad zone of ~180 m thickness in which the amplitudes of the reflectors were significantly reduced. They proposed that finely dispersed gas hydrate reduced the reflection coefficients and estimated an average hydrate filled pore volume of 3–10% in this hydrate-bearing zone. Hydrate concentrations calculated in our model are one order of magnitude lower than this rough estimate. If the estimate based on seismic data would hold, the model would imply that less than 10% of the hydrate accumulating in the slope deposits is formed by the degradation of organic matter within the hydrate stability zone. More than 90% would be delivered to the near-surface sediments by methane ascending from deeper layers. In the northern Sakhalin slope area numerous gas escape structures were imaged using seismic techniques (Lüdmann and Wong, 2003). Seafloor observations, hydro-acoustic surveys, and methane measurements in the water column showed that gas bubbles are released in the northern slope area at more than 100 different locations (Obzhirov et al., 2004; Shoji et al., 2005). At these sites gas hydrates are found in shallow surface sediments (Ginsburg et al., 1993; Matveeva et al., 2003). It thus seems to be likely that most of the hydrates accumulating within the HSZ of the northern Sakhalin slope are formed by gas bubbles ascending from deep sedimentary layers situated below the BSR.

6. Conclusions

The new kinetic rate law of organic matter degradation presented and successfully tested in this paper has profound implications for microbial degradation processes in deep anoxic marine sediments. The rate law predicts that organic matter degradation is severely hindered in anoxic sediments where high dissolved metabolite concentrations accumulate while organic matter of the same age may be degraded at a considerably higher rate if the dissolved metabolites (DIC and methane) are removed from the system. Degradation should thus proceed more rapidly in sediments with high porosity since dissolved species are rapidly lost to the overlying water by molecular diffusion in these "open" systems. Ancient organic matter conserved over extended periods of time in deep sediment layers may also be degraded when the diffusive loss is promoted by low modern depositional rates or the erosion of surface sediments. The removal of dissolved metabolites by seawater inflow and sediment reworking (erosion and re-deposition) should also enhance microbial degradation rates.

In contrast to other more detailed models of microbial respiration (Jin and Bethke, 2003) and organic matter degradation (Wirtz, 2003), the new empirical rate law does not resolve the complex microbial mechanisms involved in the anaerobic degradation of organic matter. It has rather been designed as a simple tool for the prognostic modeling of organic matter degradation, sulfate reduction and methane formation in anoxic sediments on large spatial and temporal scales. The model is based on the age-dependent kinetics introduced by Middelburg (1989) and converges to this model at low metabolite concentrations. Thus, the degradation rates in fully anoxic sediments with DIC and CH_4 concentrations of 100 mM, each, are reduced by 85% through metabolite inhibition whereas degradation in oxic sediments with DIC concentration of 2 mM are diminished by only 5% through the new inhibition term at a given POC concentration and sediment age. As the original age-dependent model has been tested and calibrated over a wide range of sedimentary environments, the new model should also correctly predict organic matter degradation in other settings such as oxic deposits at the deep-sea floor. It is, however, not well suited to predict organic matter degradation rates within the top 10 cm of the sediment column, since the age of organic matter is not well defined in these bioturbated surface layers.

The new rate law predicts that most of the hydrates found in marine sediments are not formed by organic matter degradation within the hydrate stability zone but rather by the ascent of fluids and gases. Significant concentrations of gas hydrates (>1 vol%) may thus only accumulate where fluids or methane gas bubbles originating from deeper

sediment layers are transported into the hydrate stability zone. Recent model estimates of the global hydrate abundance rely heavily on the kinetic rate law of organic matter degradation applied in the modeling procedure (Buffett and Archer, 2004; Archer and Buffett, 2005). Our model results show that the rates of methane formation in the hydrate stability zone have been over-estimated by these previous models. Hence, the new rate law presented in this paper would yield much lower estimates of the global hydrate abundance if applied in this model concept. It should however be noted that gas ascent from below the BSR was not considered in these previous models (Buffett and Archer, 2004) while our analysis of the Blake Ridge and Sakhalin slope data implies that gas ascent could be a common process at many continental margin sites.

Sediment temperature may also affect the rate of microbial methane generation. Wellsbury et al. (1997) showed that the microbial production of acetate is dramatically increased when sediments are heated. The highest acetate production was observed at temperatures of 20–60 °C and field data from Blake Ridge showed that most of the methane generated below the BSR is formed by microorganisms using acetate as substrate. Temperatures within the HSZ are usually lower than 20 °C. Considering an average thermal gradient of 30 ° km^{-1}, the experiments imply that methane production may be much higher in deeper sediment layers (~0.5–2 km depth) underlying the HSZ. Field data demonstrate that free gas produced in these deep layers may ascend to the surface to form gas hydrates. The conditions allowing for the rise of gas bubbles through sediments are, however, poorly understood. It is usually assumed that an interconnected network of gas bubbles occupying at least 10% of the pore space has to be formed to fracture the sediment and drive gas towards the seafloor (Buffett and Archer, 2004). New experimental studies show, however, that fine grained sediments act as elastic solids which are easily fractured by individual gas bubbles (Boudreau et al., 2005). It may thus be possible that gas bubbles rise to the surface without forming an interconnected network in the subsurface source area. Current estimates of the regional and global abundance of gas hydrates are not reliable because the methane production rates in deep and warm sediment layers underlying the HSZ are unknown and the upward transport of methane into the HSZ has only been studied at very few locations. More reliable model-based estimates will only emerge after the temperature effect on microbial methane formation and the mechanisms of gas bubble ascent through sediments have been studied in more detail.

Acknowledgments

The captains and crew members of the research vessels *Akademik Lavrentyev* and *Sonne* provided helpful assistance at sea, their work is greatly appreciated. We would like to thank N. Biebow for organizing the cruises and E. Suess for initiating our work in the Sea of Okhotsk. Special thanks go to Bettina Domeyer, Anke Bleyer, and Regina Surberg for having carried out the chemical analyses. The helpful comments of two anonymous reviewers and B. Buffett are greatly appreciated. This work was funded by the BMBF within the framework of the German-Russian KOMEX project (Grant 03G0534A).

Associate editor: Jack J. Middelburg

Appendix A. Modeling procedure used in the evaluation of the Sea of Okhotsk data

In the following, details of the modeling procedure are presented and discussed while model equations are summarized in Tables A1–A3. All depth-dependent variables are listed in Table A1. Porosity is assumed to decay exponentially with depth (x) due to steady-state compaction

Table A1
Depth-dependent constitutive equations used in the modeling

Parameter	Constitutive equation
Porosity	$\Phi = \Phi_f + (\Phi_0 - \Phi_f) \cdot e^{-p \cdot x}$
Molecular diffusion in sediments	$D_S = \Phi^2 \cdot D_M$
Burial of solids	$w = \frac{w_f \cdot (1-\Phi_f)}{1-\Phi}$
Burial of pore water	$v = \frac{\Phi_f \cdot w_f}{\Phi}$
Age-dependent kinetic constant for POM degradation	$k_x = 0.16 \cdot \left(a_0 + \frac{x}{w}\right)^{-0.95}$
Factor converting G (wt%) in C (mmol cm^{-3})	$r = \frac{10 \cdot d_S \cdot (1-\Phi)}{MW \cdot \Phi}$

Table A2
Rate laws used in the modeling

Rate	Kinetic rate law
Sulfate reduction	$R_{SR} = 0.5 \cdot \frac{C(SO_4)}{C(SO_4)+K_{SO_4}} \cdot r(POC) \cdot R_{POC}$
Methanogenesis	$R_M = 0.5 \cdot \frac{K_{SO_4}}{C(SO_4)+K_{SO_4}} \cdot r(POC) \cdot R_{POC}$
Anaerobic oxidation of methane	$R_{AOM} = k_{AOM} \cdot C(SO_4) \cdot C(CH_4)$
PON degradation	$R_{PON} = \frac{14}{12} \cdot \frac{16}{106} \cdot R_{POC}$
Ammonium adsorption	$R_{ADS} = k_{ADS} \cdot (1 - \frac{ADS}{C(NH_4) \cdot K_{ADS}})$
$CaCO_3$ precipitation	$R_{CaCO_3} = k_{CaCO_3} \cdot (C(Ca) - C(Ca)_{OBS})$

Table A3
Rate expressions applied in the differential equations

Species	Rates
Particulate organic carbon (POC)	$R(POC) = -R_{POC}$
Particulate organic nitrogen (PON)	$R(PON) = -R_{PON}$
Adsorbed ammonium (ADS)	$R(ADS) = +R_{ADS} \cdot \frac{d_S \cdot (1-\Phi)}{\Phi}$
Sulfate (SO_4)	$R(SO_4) = -R_{SR} - R_{AOM}$
Methane (CH_4)	$R(CH_4) = +R_M - R_{AOM}$
Bromide (Br)	$R(Br) = +r_{Br} \cdot r(POC) \cdot R_{POC}$
Ammonium (NH_4)	$R(NH_4) = +r(PON) \cdot R_{PON} - R_{ADS}$
Iodide (I)	$R(I) = +r_I \cdot r(POC) \cdot R_{POC}$
Dissolved inorganic carbon ($DIC = CO_3^{2-} + HCO_3^- + CO_2$)	$R(DIC) = +r(POC) \cdot R_{POC} + R_{AOM} - R_M - r(CaCO_3) \cdot R_{CaCO_3}$
Calcium (Ca)	$R(Ca) = -r(CaCO_3) \cdot R_{CaCO_3}$

(Berner, 1980) where the initial porosity at zero depth (Φ_0), the porosity at infinite depth (Φ_f), and the attenuation coefficient (p) are derived from the data applying non-linear fitting techniques. Molecular diffusion coefficients (D_M) are calculated for the prevailing temperature (2 °C) and salinity (35) using equations given in Boudreau (1997). Dissolved inorganic carbon (DIC) is transported using the diffusion coefficient of HCO_3 because bicarbonate is the major DIC species at the near-neutral pH conditions prevailing in anoxic sediments. Archie's law is applied to consider the effects of tortuosity on diffusion and to calculate the coefficients for diffusion in sediments (D_S). The applied coefficient (Φ^2 corresponding to $m = 3$ in Archie's law) is a good approximation for the fine-grained and water-rich sediments of the study area (Ullman and Aller, 1982). Burial of solids and pore water is calculated considering steady-state compaction (Berner, 1980). Sedimentation rates (w_f) are calculated using nitrogen mass balances as outlined in Section 4. The age-dependent kinetic constant for POC degradation is taken from Middelburg (1989) while the initial age (a_0) is determined by fitting the model to the data. Concentrations of dissolved species (C in mmol cm^3 of pore water) are related to the corresponding concentrations of solid species (G given in wt%) using conversion factors (r) which include the depth-dependent porosity, the average density of dry solids ($d_s = 2.5$ g cm^{-3}) and the appropriate molecular weights (MW) of C and N. These factors are applied to calculate the release and consumption of solutes resulting from the turnover of solids (Tables A2 and A3).

Kinetic rate laws are defined using Monod kinetics and applying appropriate stoichiometric coefficients (Table A2). The rate of sulfate reduction is related to the POC degradation rate (R_{POC}) considering that reduction rates decrease at very low sulfate concentrations ($K_{SO_4} = 1$ mM). Methane formation is inhibited in the presence of sulfate and is driven by POC degradation. The anaerobic oxidation of methane (AOM) is assumed to follow second order kinetics depending on both sulfate and methane concentrations (Luff and Wallmann, 2003). The value of the kinetic constant (k_{AOM}) is defined by fitting the model to the sulfate and methane data. Degradation of particulate organic nitrogen (PON) is linked to POC degradation considering Redfield stoichiometry and the appropriate N:C weight ratio (14/12).

Ammonium adsorption can be modeled as a linear equilibrium reaction where the depth-independent equilibrium constant K_{ADS} is defined as the ratio between adsorbed ammonium (ADS in mmol NH_4 (g dry solids)$^{-1}$) and dissolved ammonium ($C(NH_4)$ in mmol NH_4 (cm^3 pore water)$^{-1}$) at equilibrium (Berner, 1980). In fine-grained marine sediments K_{ADS} attains a value of 1.7 cm^3 g^{-1} (Mackin and Aller, 1984). We prefer to model ammonium adsorption using a kinetic approach because the equilibrium approach would demand the use of rather complicated differential-algebraic equations. The kinetic constant is, however, set to a large value ($k_{ADS} = 1$ mM yr^{-1}) so that equilibrium between dissolved and adsorbed ammonium is always maintained ($ADS/C(NH_4) = K_{ADS}$).

Carbonate precipitation in anoxic sediments has been modeled successfully by different authors using numerically rather demanding procedures (Luff and Wallmann, 2003; Luff et al., 2004). It is controlled by pH and saturation states of pore waters which are calculated only with a considerable numerical effort (Boudreau, 1987; Van Cappellen and Wang, 1996). Here, we prefer to use a rather simple approach to avoid extensive integration times. Carbonate precipitation is driven by the measured calcium concentrations in pore water. For this purpose appropriate functions are fitted through the Ca data to obtain representative concentrations for each depth interval ($C(Ca)_{OBS}$). The rate is set proportional to the difference between modeled ($C(Ca)$) and measured concentrations ($C(Ca)_{OBS}$) and a large value is assigned to the corresponding kinetic constant ($k_{CaCO3} = 0.05$ wt% $CaCO_3$ yr^{-1}) so that concentrations calculated in the model are always very close to measured values.

Reaction rates are combined appropriately to define reaction terms which are applied in the differential equations for each solid and dissolved species (Table A3). Conversion factors (r) are introduced to maintain the correct dimensions for solid and dissolved species concentrations. Stoichiometric coefficients are used to derive the release rates of metabolites (ammonium, bromide, and iodide) from POC degradation rates. Finally, the reaction terms are combined with other terms describing the transport of solids and solutes (see Section 4) and the resulting system of differential equations is solved to calculate the concentration–depth profiles of 10 species at steady-state.

Appendix B. Modeling of gas hydrate formation

The model described in Appendix A was extended and modified in order to simulate gas hydrate formation at Black Ridge (ODP Site 997) and in Sakhalin slope deposits (Table A4). Since the model columns extend over several 100 m, the effect of sediment temperature on diffusion was considered. Molecular diffusion coefficients were calcu-

Table A4
Equations used in the modeling of gas hydrate formation

Parameter	Constitutive equation
Molecular diffusion in sediments	$D_S = \frac{D_M}{1-2\cdot\ln(\Phi)}$
Upward fluid flow and pore water burial	$v = \frac{\Phi_f \cdot w_f - v_0 \cdot \Phi_0}{\Phi}$
Rate of hydrate formation If $\left[\frac{C(CH_4)}{C_{SAT}} > 1\right]$	$R_{GH} = k_{GH} \cdot \left(\frac{C(CH_4)}{C_{SAT}} - 1\right)$
Rate of hydrate dissolution If $\left[\frac{C(CH_4)}{C_{SAT}} \leqslant 1\right]$	$R_{GHD} = k_{GHD} \cdot \left(1 - \frac{C(CH_4)}{C_{SAT}}\right) \cdot G(GH)$
Factor converting wt% in vol%	$r_{GH} = \frac{d_S \cdot (1-\Phi)}{d_{GH} \cdot \Phi}$

lated as a function of sediment temperature (Boudreau, 1997) and hence increased with sediment depth. Moreover, the effect of porosity on diffusion was considered using the logarithmic equation given by (Boudreau, 1996a) rather than applying Archie's Law since the former equation is valid over a wider range of sediment compositions and porosities (Boudreau, 1997). Dissolved inorganic carbon (DIC) was transported applying the mean diffusion coefficient of HCO_3^- and CO_2 since CO_2 is a major species under the acidic conditions prevailing in deep methanogenic sediments. Upward fluid flow was considered in the Blake Ridge simulation, only, using the approach described in Luff and Wallmann (2003). The interstitial velocity at zero depth (v_0) was varied to fit the pore water data.

Gas hydrate was precipitated from the pore solution when the concentration of dissolved methane calculated in the model surpassed the solubility of gas hydrates (C_{SAT}). We used a kinetic approach to simulate hydrate precipitation and dissolution (Torres et al., 2004) and a modified Pitzer-approach for the calculation of hydrate solubility (Tishchenko et al., 2005). The kinetic constant for hydrate precipitation was set to a large value ($k_{GH} = 2 \times 10^{-2}$ wt% yr^{-1}) to prevent over-saturation with respect to gas hydrate. Hydrates were allowed to dissolve in under-saturated pore solutions applying a corresponding kinetic constant of $k_{GHD} = 2 \times 10^{-2}$ wt% yr^{-1}. Hydrate concentrations (G(GH)) were initially calculated in wt% and were subsequently converted into percent of pore volume filled by hydrate considering the density of dry sediments ($d_s = 2.5$ g cm^{-3}) and gas hydrates ($d_{GH} = 0.916$ g cm^{-3}).

Boundary conditions for dissolved species applied at the base of the model column have a strong effect on the amount of hydrate formed in the model sediments. At Blake Ridge, we prescribed constant concentrations at the base of the hydrate stability zone corresponding to the values measured at that depth (451 m). Only for dissolved methane, the lower boundary value was calculated assuming equilibrium with pure methane gas hydrate (type I, Tishchenko et al., 2005). In the prognostic modeling of hydrate formation in Sakhalin slope deposits, we applied constant gradient conditions for SO_4, DIC, and CH_4 Eq. (12). With this approach methane and DIC continuously produced in deeper sediment sections situated below the base of the model column (300 m), is allowed to enter the model domain via molecular diffusion.

References

Aloisi, G., Wallmann, K., Drews, M., Bohrmann, G., 2004. Evidence for the submarine weathering of silicate minerals in Black Sea sediments: possible implications for the marine Li and B cycles. *Geochem. Geophys. Geosyst.* **5** (4), Q04007, 10.1029/2003GC000639.

Antoine, D., André, J.-M., Morel, A., 1996. Oceanic primary production 2. Estimation of global scale from satellite (coastal zone color scanner) chlorophyll. *Global Biogeochem. Cycles* **10** (1), 57–69.

Archer, D., Buffett, B., 2005. Time-dependent response of the global ocean clathrate reservoir to climatic and anthropogenic forcing. *Geochem. Geophys. Geosyst.* **6** (3), 10.1029/2004GC000854.

Berner, R.A., 1980. *Early Diagenesis—A Theoretical Approach*. Princeton University Press.

Biebow N. and Hütten E. 2000. KOMEX Cruise Reports. GEOMAR Research Center.

Boudreau, B.B., Canfield, D.E., 1993. A comparison of closed- and open-system models for porewater pH and calcite-saturation state. *Geochim. Cosmochim. Acta* **57**, 317–334.

Boudreau, B.B., Ruddick, B.R., 1991. On a reactive continuum representation of organic matter diagenesis. *Am. J. Sci.* **291**, 507–538.

Boudreau, B.P., 1987. A steady-state diagenetic model for dissolved carbonate species and pH in the pore waters of oxic and suboxic sediments. *Geochim. Cosmochim. Acta* **51**, 1985–1996.

Boudreau, B.P., 1996a. The diffusive tortuosity of fine-grained unlithified sediments. *Geochim. Cosmochim. Acta* **60** (16), 3139–3142.

Boudreau, B.P., 1996b. A method-of-lines code for carbon and nutrient diagenesis in aquatic sediments. *Comput. Geosci.* **22** (5), 479–496.

Boudreau, B.P., 1997. *Diagenetic Models and Their Implementation*. Springer-Verlag.

Boudreau, B.P., Algar, C., Johnson, B.D., Croudace, I., Reed, A., Furukawa, Y., Dorgan, K.M., Jumars, P.A., Grader, A.S., Gardiner, B.S., 2005. Bubble growth and rise in soft sediments. *Geology* **33** (6), 517–520.

Broerse, A.T.C., Ziveri, P., Honjo, S., 2000. Coccolithophore (-$CaCO_3$) flux in the Sea of Okhotsk: seasonality, settling and alteration processes. *Mar. Micropaleontol.* **39**, 179–200.

Buffett, B., Archer, D., 2004. Global inventory of methane clathrate: sensitivity to changes in the deep ocean. *Earth Planet. Sci. Lett.* **227**, 185–199.

Davie, M.K., Buffett, B.A., 2001. A numerical model for the formation of gas hydrate below the seafloor. *J. Geophys. Res.* **106** (B1), 497–514.

Davie, M.K., Buffett, B.A., 2003a. Sources of methane for marine gas hydrate: inferences from a comparison of observations and numerical models. *Earth Planet. Sci. Lett.* **206**, 51–63.

Davie, M.K., Buffett, B.A., 2003b. A steady state model for marine hydrate formation: constraints on methane supply from pore water sulfate profiles. *J. Geophys. Res.* **108** (B10), 2495. doi:10.1029/2002JB002300.

Dickens, G.R., O'Neil, J.R., Rea, D.K., Owen, R.M., 1995. Dissociation of oceanic methane hydrate as a cause of the carbon isotope excursion at the end of the Paleocene. *Paleoceanography* **10** (6), 965–971.

Dickens, G.R., Pauli, C.K., Wallace, P., Party, t.O.L.S., 1997. Direct measurement of in situ methane quantities in a large gas-hydrate reservoir. *Nature* **385**, 426–428.

Dullo, W.-C., Biebow, N., and Georgeleit, K. 2004. SO178 KOMEX Cruise Report, IFM-GEOMAR, pp. 125.

Egeberg, P.K., Dickens, G.R., 1999. Thermodynamics and pore water halogen constraints on gas hydrate distribution at ODP Site 997 (Blake Ridge). *Chem. Geol.* **153**, 53–79.

Einsele, G., 2000. *Sedimentary Basins: Evolution, Facies, and Sediment Budget*. Springer.

Elderfield, H., Truesdale, V.W., 1980. On the biophilic nature of iodine in seawater. *Earth Planet. Sci. Lett.* **50**, 105–114.

Flemings, P.B., Liu, X., Winters, W.J., 2003. Critical pressure and multiphase flow in Blake Ridge gas hydrates. *Geology* **31** (12), 1057–1060.

Fossing, H., Ferdelman, T.G., Berg, P., 2000. Sulfate reduction and methane oxidation in continental margin sediments influenced by irrigation (South-East Atlantic off Namibia). *Geochim. Cosmochim. Acta* **64** (5), 897–910.

Ginsburg, G.D., Soloviev, Cranston, R.E., Lorenson, T.D., Kvenvolden, K.A., 1993. Gas hydrates from the continental slope, offshore Sakhalin Island, Okhostk Sea. *Geo-Mar. Lett.* **13**, 41–48.

Gorbarenko, S.A., Nürnberg, D., Derkachev, A.N., Astakhov, A.A., Southon, J.R., Kaiser, A., 2002. Magnetostratigraphy and tephrochronology of the Upper Quaternary sediments in the Okhotsk Sea: implication of terrigenous, volcanogenic and biogenic matter supply. *Mar. Geol.* **183**, 107–129.

Gorman, A.R., Holbrook, W.S., Hornbach, M.J., Hackwith, K.L., Lizarralde, D., Pecher, I., 2002. Migration of methane gas through the hydrate stability zone in a low-flux hydrate province. *Geology* **30** (4), 327–330.

Grasshoff, K., Ehrhardt, M., Kremling, K., 1983. *Methods of Seawater Analysis*. Verlag Chemie.

Hedges, J.H., Hu, F.S., Devol, A.H., Hartnett, H.E., Tsamakis, E., Keil, R.G., 1999. Sedimentary organic matter preservation: a test for selective degradation under oxic conditions. *Am. J. Sci.* **299**, 529–555.

Hensen, C., Zabel, M., Pfeifer, K., Schwenk, T., Kasten, S., Riedinger, N., Schulz, H.D., Boetius, A., 2003. Control of sulfate pore-water profiles by sedimentary events and the significance of anaerobic oxidation of methane for the burial of sulfur in marine sediments. *Geochim. Cosmochim. Acta* **67** (14), 2631–2647.

Ivanenkov, V.N., Lyakhin, Y.I., 1978. Determination of total alkalinity in seawater. In: Bordovsky, O.K., Ivanenkov, V.N. (Eds.), *Methods of Hydrochemical Investigations in the Ocean*. Nauka Publ. House, pp. 110–114, in Russian.

Jin, Q., Bethke, C.M., 2003. A new rate law describing microbial respiration. *Appl. Environ. Microbiol.* **69** (4), 2340–2348.

Jørgensen, B.B., Weber, A., Zopfi, J., 2001. Sulfate reduction and anaerobic methane oxidation in Black Sea sediments. *Deep-Sea Res. I* **48**, 2097–2120.

Kennedy, H.A., Elderfield, H., 1987. Iodine diagenesis in pelagic deep-sea sediments. *Geochim. Cosmochim. Acta* **51**, 2489–2504.

Kristensen, E., Holmer, M., 2001. Decomposition of plant materials in marine sediment exposed to different electron acceptors (O_2, NO_3^-, and SO_4^{2-}), with emphasis on substrate origin, degradation kinetics, and the role of bioturbation. *Geochim. Cosmochim. Acta* **65** (3), 419–433.

Kvenvolden, K.A., Lorenson, T.D., 2001. The global occurrence of natural gas hydrate. *Geophys. Monogr.* **124**, 87–98.

Lüdmann, T., Wong, K.K., 2003. Characteristics of gas hydrate occurrences associated with mud diaprism and gas escape structures in the northwestern Sea of Okhotsk. *Mar. Geol.* **201**, 269–286.

Luff, R., Wallmann, K., 2003. Fluid flow, methane fluxes, carbonate precipitation and biogeochemical turnover in gas hydrate-bearing sediments at Hydrate Ridge, Cascadia Margin: numerical modeling and mass balances. *Geochim. Cosmochim. Acta* **67** (18), 3403–3421.

Luff, R., Wallmann, K., Aloisi, G., 2004. Numerical modeling of carbonate crust formation at cold vent sites: significance for fluid flow and methane budgets and chemosynthetic biological communities. *Earth Planet. Sci. Lett.* **221**, 337–353.

Luff, R., Wallmann, K., Grandel, S., Schlüter, M., 2000. Numerical modelling of benthic processes in the deep Arabian Sea. *Deep-Sea Res. II* **47** (14), 3039–3072.

Mackin, J.E., Aller, R.C., 1984. Ammonium adsorption in marine sediments. *Limnol. Oceanogr.* **29** (2), 250–257.

Maher, K., DePaolo, D.J., Lin, J.C.-F., 2004. Rates of silicate dissolution in deep-sea sediment: in situ measurement using $^{234}U/^{238}U$ of pore fluids. *Geochim. Cosmochim. Acta* **68** (22), 4629–4648.

Martin, J.B., Gieskes, J.M., Torres, M., Kastner, M., 1993. Bromine and iodine in Peru margin sediments and pore fluids: implications for fluid origins. *Geochim. Cosmochim. Acta* **57**, 4377–4389.

Matveeva, T., Soloviev, V., Wallmann, K., Obzhirov, A., Biebow, N., Poort, J., Salomatin, A., Shoji, H., 2003. Geochemistry of gas hydrate accumulation offshore NE Sakhalin Island (the Sea of Okhotsk): results from the KOMEX-2002 cruise. *Geo-Mar. Lett.* **23**, 278–288.

Middelburg, J.J., 1989. A simple model for organic matter decomposition in marine sediments. *Geochim. Cosmochim. Acta* **53**, 1577–1581.

Milkov, A.V., 2004. Global estimates of hydrate-bound gas in marine sediments: how much is really out there? *Earth Sci. Rev.* **66** (3-4), 183–197.

Niewöhner, b., Hensen, C., Kasten, S., Zabel, M., Schulz, H.D., 1998. Deep sulfate reduction completely mediated by anaerobic methane oxidation in sediments of the upwelling area off Namibia. *Geochim. Cosmochim. Acta* **62** (3), 455–464.

Obzhirov, A., Shakirov, R., Salyuk, A., Suess, E., Biebow, M., Salomatin, A., 2004. Relations between methane venting, geological structure and seismo-tectonics in the Okhotsk Sea. *Geo-Mar. Lett.* **24**, 135–139.

Paull C. K., Matsumoto R., Wallace P. J., Dillon W. P., 2000. Proceedings of the Ocean Drilling Program, Scientic Results, Vol. 164.

Rabouille, C., Gaillard, J.-F., 1991. Towards the EDGE: early diagenetic global explanation. A model depicting the early diagenesis of organic matter, O_2, NO_3, Mn, and PO_4. *Geochim. Cosmochim. Acta* **55**, 2511–2525.

Rempel, A.W., Buffett, B.A., 1998. Mathematical models of gas hydrate accumulation. In: Henriet, J.-P., Mienert, J. (Eds.), *Gas Hydrates: Relevance to World Margin Stability and Climate Change*, vol. 137. Geological Society, pp. 63–74.

Sayles, F.L., Mangelsdorf Jr., P.C., 1977. The equilibration of clay minerals with seawater. *Geochim. Cosmochim. Acta* **41**, 951–960.

Schlitzer, R., 2000. Applying the adjoint method for biogeochemical modeling: export of particulate organic matter in the world ocean. In: Kasibhatla, P., Heimann, M., Rayner, P., Mahowald, N., Prinn, R.G., Hartley, D.E. (Eds.), *Inverse Methods in Global Biogeochemical Cycles*, Vol. 114. American Geophysical Union, pp. 107–124.

Shoji, H., Soloviev, V., Matveeva, T., Mazurenko, L., Minami, H., Hachikubo, A., Sakagami, H., Hyakutake, K., Kaulio, V., Gladysch, V., Logvina, E., Obzhirov, A., Baranov, B., Khlystov, O., Biebow, N., Poort, J., Jin, Y.K., Kim, Y., 2005. Hydrate-bearing structures in the sea of Okhotsk. *EOS* **86** (2), 13/18.

Tishchenko, P., Hensen, C., Wallmann, K., Wong, C.S., 2005. Calculation of the stability and solubility of methane hydrate in seawater. *Chem. Geol.* **219**, 37–52.

Torres, M.E., Wallmann, K., Trehu, A.M., Bohrmann, G., Borowski, W.S., Tomaru, H., 2004. Gas hydrate growth, methane transport, and chloride enrichment at the southern summit of Hydrate Ridge, Cascadia margin off Oregon. *Earth Planet. Sci. Lett.* **226**, 225–241.

Tromp, T.K., Cappellen, P.V., Key, R.M., 1995. A global model for the early diagenesis of organic carbon and organic phosphorus in marine sediments. *Geochim. Cosmochim. Acta* **59** (17), 1259–1284.

Ullman, W.J., Aller, R.C., 1982. Diffusion coefficients hin near-shore marine sediments. *Limnol. Oceanogr.* **27**, 552–556.

Van Cappellen, P., Wang, Y., 1996. Cycling of iron and manganese in surface sediments: a general theory for the coupled transport and reaction of carbon, oxygen, nitrogen, sulfur, iron, and manganese. *Am. J. Sci.* **296**, 197–243.

Wallmann, K., Linke, P., Suess, E., Bohrmann, G., Sahling, H., Schlüter, M., Dählmann, A., Lammers, S., Greinert, J., von Mirbach, N., 1997. Quantifying fluid flow, solute mixing, and biogeochemical turnover at cold vents of the eastern Aleutian subduction zone. *Geochim. Cosmochim. Acta* **61** (24), 5209–5219.

Wellsbury, P., Goodman, K., Barth, T., Cragg, B.A., Barnes, S.P., Parkes, J., 1997. Deep marine biosphere fuelled by increasing organic matter availability during burial and heating. *Nature* **388**, 573–576.

Westrich, J.T., Berner, R.A., 1984. The role of sedimentary organic matter in bacterial sulfate reduction: the G model tested. *Limnol. Oceanogr.* **29** (2), 236–249.

Wirtz, K.W., 2003. Control of biogeochemical cycling by mobility and metabolic strategies of microbes in the sediments: an integrated model study. *FEMS Microbiol. Ecol.* **46**, 295–306.

Wong, H.K., Lüdmann, T., Baranov, B.V., Karp, B.Y., Konerding, P., Ion, G., 2003. Bottom current-controlled sedimentation and mass wasting in the northwestern Sea of Okhotsk. *Mar. Geol.* **201**, 287–305.